Author version: *J. Phys. Oceanogr., vol.45(7); 2015; 1947-1966*

Seasonal Variability of salinity and salt transport in the northern Indian Ocean

Joseph M. D'Addezio[1*], Bulusu Subrahmanyam[1,2], Ebenezer S. Nyadjro[3], V.S.N. Murty[4]

[1]Marine Science Program, University of South Carolina, Columbia, SC 29208

[2]Department of Earth and Ocean Sciences, University of South Carolina, Columbia, SC 29208

[3] Department of Physics, University of New Orleans, New Orleans, LA 70148

[4]Council of Scientific and Industrial Research (CSIR) - National Institute of Oceanography Regional Centre, Visakhapatnam - 530 017, India

Journal of Physical Oceanography
May 5, 2015

***Corresponding Author:** Joseph M. D'Addezio
Email Address: jdaddezio@geol.sc.edu

Abstract

Analyses using a suite of observational datasets (Aquarius and Argo) and model simulations are carried out to examine the seasonal variability of salinity in the Northern Indian Ocean (NIO). The model simulations include the Consortium for Estimating the Circulation and Climate of the Ocean (ECCO2), European Centre for Medium-Range Weather Forecasts - Ocean Reanalysis System 4 (ECMWF-ORSA4), Simple Ocean Data Assimilation (SODA) Reanalysis, and HYbrid Coordinate Ocean Model (HYCOM). Our analyses of salinity at the surface and at depths up to 200 m, surface salt transport in the top 5 m layer, and depth-integrated salt transports revealed different salinity processes in the NIO that are dominantly related to the semi-annual monsoons. Aquarius proves a useful tool for observing this dynamic region, and reveals some aspects of sea surface salinity (SSS) variability that Argo cannot resolve. The study revealed large disagreement between surface salt transports derived from observed and analysis-derived salinity fields. Although differences in SSS between the observations and the model solutions are small, model simulations provide much greater spatial variability of surface salt transports due to finer detailed current structure. Meridional depth-integrated salt transports along 6°N revealed dominant advective processes from the surface towards near-bottom depths. In the Arabian Sea (Bay of Bengal), net monthly mean maximum northward (southward) salt transport of ~50×10^6 kg s^{-1} occurs in July, and annual mean salt transports across this section are about -2.5×10^6 kg s^{-1} (3×10^6 kg s^{-1}).

1. Introduction

The Northern Indian Ocean (NIO) exhibits a unique dipolar sea surface salinity (SSS) structure with its basin split between the salty Arabian Sea (AS) and the fresher Bay of Bengal (BoB). While both basins share the same latitude band and are affected by the semi-annually reversing monsoonal winds, their salinity structures greatly differ. The AS is dominated by higher evaporation and lower precipitation regimes and is the main outflow region for the high salinity waters of both the Red Sea and the Persian Gulf (Rao and Sivakumar, 2003). The BoB experiences much higher precipitation rates, which typically overwhelms evaporation, and also receives large amounts of fresh water runoff from some of the world's largest rivers (Sengupta et al., 2006). As the winds transition between the southwest monsoon (SWM) and northeast monsoon (NEM), the two basins exchange water around Sri Lanka (Jensen, 2001). This exchange allows the BoB to transfer excess freshwater to the AS and thereby maintain its salt balance. The transfer of salty waters into the BoB is subtler, as the denser AS waters tend to sink to ~100 m after it passes Sri Lanka and enters the Bay (Vinayachandran et al., 2013).

As noted above, the monsoon seasons play an integral role in the spatial variability of surface winds, currents, temperature, and salinity in the NIO. The NEM occurs between November and February, during which time strong northeasterly winds blow off the Indian subcontinent into the central Indian Ocean (Schott and McCreary, 2001). This pattern typically reaches its peak in January. The surface wind circulation pattern drives the Northeast Monsoon Current (NMC), which advects water from the BoB into the AS (Wyrtki, 1971; McCreary et al., 1993; Schott et al., 1994). The East Indian Coastal Current (EICC) leaves the BoB and eventually merges with the West India Coastal Current (WICC) along the pathway of the NMC (Shetye et al., 1991; Shetye et al., 1996; Schott and McCreary, 2001).

During the SWM, the surface wind circulation pattern transitions with winds flowing out of the southwest Indian Ocean onto the Indian subcontinent. This pattern typically reaches its peak in July. During this peak, a core of strong surface winds over the AS forms the Findlater Jet having its southwest-northeast (SW-NE) axis of flow from the Somali coast to the India coast (Findlater, 1969). The Southwest Monsoon Current (SMC) originates in the southward WICC, flows eastward along the southern tip of India and Sri Lanka, and then runs poleward off the east coast of Sri Lanka into the BoB (Shetye et al., 1991; Shetye et al., 1996; Schott and McCreary 2001; Shankar et al., 2002). Generally weak surface wind patterns exist over much of the NIO between these two seasons, cutting off most of the exchange between the two adjacent basins (Schott et al., 1994). The importance of this seasonal

exchange cannot be overstated, as many past studies have highlighted the dominance of horizontal advection in the salt budget of the NIO (Jensen, 2001; Han and McCreary, 2001; Jensen, 2003; Rao and Sivakumar, 2003; Vinayachandran et al., 2009; Nyadjro et al., 2011; Akhil et al., 2014).

The NIO also shows a rich vertical salinity structure. Depth profiles along the 88°E section in the BoB (Sastry et al., 1985; Shetye et al., 1996) show a variety of complexities in temperature and salinity. With respect to salinity, the northern end of the Bay is dominated by river outflow, which generates surface salinity values as low as 25 psu. This feature is very shallow and at 40 m depth the salinity abruptly jumps to ~35 psu. At approximately 40 m, several dome structures occur with high salinity cores sitting just below the dome peaks. Below 250 m, the vertical structure becomes more uniform and is unperturbed by the large influx of low salinity waters at the surface (Sastry et al., 1985; Shetye et al., 1996). This relatively high salinity layer is likely due to mixing between the AS and the BoB waters. Using monthly climatology for July, Vinayachandran et al. (2013) showed the 35 psu isohaline advected from the AS surface waters sinks down as it comes into contact with the much fresher waters of the BoB. This sinking motion begins at 50 m depth as water is advected past India and Sri Lanka and continues to sink as it spreads across the entire BoB at a depth of approximately 100 m (Murty et al., 1992). The vertical salinity structure of the AS is much more uniform, but low salinity waters from the BoB can be seen at the surface during the NEM when the exchange from the BoB is at its maximum. These waters enter the AS from the south, but are eventually carried poleward by the WICC (Shetye et al., 1991; Shankar et al., 2002). High salinity waters from the Persian Gulf spread southward and eastward between 200 and 400 m. The southward moving branch then mixes with the highly saline Red Sea watermass that typically lies between 400 and 800 m (Prasannakumar and Prasad, 1996).

While the Indian Ocean's important contribution to global salt and heat budgets is well known to the scientific community, quantified analyses of its physical dynamics are underrepresented in the literature. The almost 3 year record provided by Aquarius gives us reason to reexamine this seasonally variable region with the aid of this new observational dataset as well as analyze how the satellite-derived SSS compares with the Argo floats data and the numerous model simulations frequently used to investigate the area. Additionally, many studies focusing on this region of the ocean may only use one or two products to give quantitative estimates of variables such as depth-integrated transports, a quantity that is difficult to capture by observations on a large scale. We take the opportunity to use several different datasets to quantify salinity processes over the entire water column and compare their results.

This will provide a useful comparison tool for future researchers using Aquarius, Argo, these modeled products, or a combination of them all.

Figure 1 shows the mean Aquarius SSS during August 2011-May 2014 and several box-averaging regions that were selected for examining various aspects of the salinity within the NIO. These sub-regions are chosen based on the differing physical dynamics of the NIO as a whole. In this study we first examine the seasonal SSS anomalies during each monsoon season using Aquarius, Argo, and the modeled products to better understand how Aquarius compares to these previously utilized datasets and how it can be a useful tool for understanding this region. Because the seasonal advective processes in this region are so strong and dynamic, surface salt transports will be quantified using both the observations and the modeled products. Next we investigate the seasonal and year-to-year variability of salinity below the surface by using the aforementioned regional boxes to generate box-averaged salinity versus depth profiles. Finally, model simulations and reanalysis products are used to quantify meridional depth-integrated salt transports at the 6°N cross-section in both the AS and BoB. Many earlier intercomparison studies using reanalysis products (e.g. Gemmell et al., 2008; Lee et al., 2009; Munoz et al., 2011) focused on the ocean state, but not the transport estimates. This allows greater understanding of the total salt flux across this latitudinal boundary of each basin, the major flow patterns into and out of each that generates seasonal and longitudinal variability in their respective transport profiles, and how the results using each dataset compare to one another.

2. Data and Methods

2.1 Models and Reanalyses

In this study, we use outputs from four model-based analyses: the Consortium for Estimating the Circulation and Climate of the Ocean (ECCO2), the European Centre for Medium-Range Weather Forecasts - Ocean Reanalysis System 4 (ECMWF-ORAS4), Simple Ocean Data Assimilation (SODA v2.2.4) Reanalysis and the HYbrid Coordinate Ocean Model (HYCOM v2.2.19). We have chosen these different products to exploit their different base models, assimilation methods, choice of initial conditions, surface forcings, and resolutions, summaries of which are provided in Table 1. ECCO2, ORAS4, and SODA are ocean reanalysis products (Carton and Giese, 2008; Menemenlis et al., 2008; Balmaseda et al., 2013). The version of HYCOM that we used here assimilates observational data including the riverine run off from many rivers in the NIO (Chassignet et al., 2003; Metzger et al.,

2014). The vertical resolutions of all the products are usually finer in the surface layers (~10 m) and increase in deeper layers (~500 m).

With the Indian Ocean suffering from sparse availability of observational data, models of the region have the potential of systematic biases (http://www.tropmet.res.in/monsoon/files/model_biases.php). The models used in this study assimilate similar *in-situ* and satellite-derived data (e.g. from Argo, XBT and altimetry; Table 1), however, the sources and quality-controlled procedures applied are not identical and hence can cause differences among the model outputs (Lee et al., 2009). XBT data, for example, often contain a warm bias as a result of inaccurate modeling of the instrument fall rate. The SODA products correct this bias using the methods of Hanawa et al. (1995) while the ORAS4 products use the methods of Wijffels et al. (2009). The atmospheric reanalysis products (e.g., the NCEP/NCAR reanalysis, ECMWF, ERA-40, and ERA-Interim reanalysis) used to force these models are also based on different models and assimilation methods, which can contribute to differences among the model products. For example, the wind forcing used in ECCO2 is a weighted mean (using a Green's function method) of satellite-derived wind products, NCEP/NCAR, and ERA-40 reanalysis products (Lee et al., 2009). ORAS4 is forced by atmospheric-derived daily surface fluxes of solar radiation, total heat flux, E-P, and surface wind stress from ERA-Interim reanalysis (Dee et al., 2011) from January 1989 to December 2009 and the ECMWF operational archive from January 2010 onward (Balmaseda et al., 2013). Differences in the models' resolutions may be important in causing differences in the comparisons of salinity, currents, and transports (Lee et al., 2009).

We also use the Coriolis Ocean database for Reanalysis (CORA v3.4) and the Ocean Surface Current Analyses Real-Time (OSCAR) datasets. CORA v3.4 data with a spatial resolution of 0.5° × 0.5° are obtained from the Coriolis Data Center (http://www.coriolis.eu.org/Science/Data-and-Products/CORA v3.4). CORA v3.4 is produced by objective analysis of in-situ temperature and/or salinity profiles obtained mainly from Argo floats, XBTs, CTDs and XCTDs, sea mammal data, and moorings (Cabanes et al., 2013). The creation of the CORA v3.4 dataset includes duplicate checks to ensure the individual input data is unique in the dataset, and various quality checks that help eliminate bad data and outliers. The Argo data inputs do not undergo any supplemental corrections while the XBTs data biases are adjusted following the methods of Hamon et al. (2012).

The OSCAR analysis uses real-time satellite altimetry and wind stress to calculate zonal and meridional surface velocities (Bonjean and Lagerloef, 2002). When compared to Lagrangian drifter data,

OSCAR performs quite well with the exception of a small underestimation of velocities due to its inability to resolve mesoscale features such as sharp sea surface height gradients (Dohan and Maximenko, 2010). Also, the NIO features a highly variable current field in both time and space (Shankar et al., 2002), which can cause the OSCAR output to be inferior to that of the higher resolution model solutions even though it is based off satellite-derived observations. Here we use monthly OSCAR absolute surface zonal and meridional velocities for January 2008 – May 2014 which has a horizontal resolution of 1°x1°.

2.2 Observations

Whenever possible Aquarius SSS and Argo floats salinity data are used to assess the relative accuracy of the model products used in this study. We used the latest Aquarius version 3.0 smoothed, monthly L3 SSS data. This data set is available on a horizontal resolution of 1°x1°, and though it is coarse, this resolution is sufficient and capable of resolving the major synoptic scale salinity features across the NIO. We obtained the International Pacific Research Centre (IPRC) processed Argo data (http://apdrc.soest.hawaii.edu/projects/argo/) with a horizontal resolution of 1°x1° and 27 vertical levels ranging from the surface to 2000 m between January 2008-May 2014. The Lagrangian nature of Argo floats can make it difficult to consistently monitor semi-enclosed basins such as the AS and BoB. Between January 2008 and May 2014, the NIO (0-30°N, 40-100°E) was sampled 56,490 times with an average distance between floats of 225 km. Because of this relatively low float density, the IPRC uses optimal interpolation to produce a final high-resolution gridded product for distribution (Lebedev et al., 2007). Schiller et al. (2004) concluded that to accurately quantify seasonal dynamics within the Indian Ocean, distances between the average float profiles needed to be limited to between 100 and 500 km. With an average spatial resolution of ~200 km in the NIO and a time in between samples of 10 days, the current state of the Argo floats program is sufficient to monitor seasonal variability in the NIO caused by the semi-annual monsoons. Nonetheless, some of the discrepancies between the Argo output and the other datasets used here could be attributed to low float density in either basin during a particular month although we hope that taking seasonal means over several years and using box average values will help mitigate this issue. Additionally, Aquarius measures salinity within only the first few centimeters of the ocean surface whereas Argo typically takes its “surface” measurement at approximately 5 m. This does create discrepancies between the products, but overall global errors are small and lie between 0.1-0.2 psu (Lagerloef et al., 2008). Finally, it should be noted that HYCOM, SODA, ECCO2, ECMWF (Table

1), and CORA v.3.4 all assimilate Argo floats data. This can make it difficult to compare the model products to Argo, as the model solutions may simply be the derivatives of the Argo output often with the assistance of higher resolutions and sophisticated physical models to generate a more robust analysis.

2.3 Methods

2.3.1 Surface Salt Transports

Surface salt transports are evaluated to estimate the horizontal advection of salt at the surface within the NIO using a variety of products. Surface meridional salt transports per unit area are estimated using the following equation (Nihashi et al., 2012; Nyadjro et al., 2013):

$$F_{sss} = \rho v SSS \qquad (1)$$

where F_{sss} is the surface salt transport per unit area in kg m^{-2} s^{-1}, ρ is the water density (1023 kg m^{-3}), v is the meridional surface velocity in m s^{-1}, and SSS is the sea surface salinity (defined in full mks units [kg kg^{-1}], i.e., the usual salinity x 10^{-3} kg g^{-1}). In the computation of zonal salt transport per unit area, v in Equation (1) is replaced with u, the zonal surface velocity in m s^{-1}. Note that this estimate is that of the absolute surface salt transport instead of the surface salt transport anomalies (Please see Jensen (2001) for the calculations and discussions of surface salt transport anomalies).

2.3.2 Mixed Layer Depth and Isothermal Layer Depth Estimation

Throughout the NIO, particularly the BoB, the formation of a barrier layer can play an important role in air-sea interactions (Masson et al., 2005; Sengupta et al., 2008; Nyadjro et al., 2012). To estimate the barrier layer thickness (BLT) in the time-depth profiles, both the mixed layer depth (MLD) and isothermal layer depth (ILD) must be quantified. MLD was calculated as the depth at which the potential density difference from the 10 dbar value is equal to the 0.2 °C threshold of de Boyer Montegut et al. (2004):

$$\Delta_\sigma = \sigma(T_{10} - 0.2, S_{10}, P_0) - \sigma(T_{10}, S_{10}, P_0) \qquad (2)$$

where T_{10} and S_{10} are respectively temperature and salinity at 10 dbar and P_0 is sea surface pressure. We have set the ILD to be the depth at which the vertical temperature profile decreases 1°C from an initial depth of 10 db.

2.3.3 Depth-integrated Salt Transports

Meridional depth-integrated salt transports are calculated to assess the amount of salt that enters and leaves each basin at 6°N on a seasonal basis. Depth-integrated salt transport is estimated following Nyadjro et al. (2011):

$$F_S = \int_{-H}^{z_o} \int_{0}^{L} \rho v(x,z) S(x,z)\, dx\, dz \qquad (3)$$

where F_s is the meridional depth-integrated salt transport in kg s^{-1}, z_o is the ocean surface, $-H$ is the maximum depth of integration which we have set to 5000 m, and L is the maximum zonal length over which the transport is integrated. The complex topography of the Indian Ocean (Figure 1) offers bathymetric constraints for which the depth-integrated transports method used in this study does not adequately capture the role of features such as sills and ridges. Nevertheless, the results obtained are generally consistent with those of previous studies.

3. Results and discussion

3.1 Seasonal Sea Surface Salinity Variability

Figure 1 shows the annual mean structure of SSS in the NIO obtained from Aquarius. The high SSS in the AS and low SSS in BoB as described in the introduction are well captured by the satellite. Figure 2 shows the seasonal SSS anomalies for both Aquarius and Argo. In January, the SSS within the AS is only slightly higher than the annual mean with positive SSS anomalies over the central and southern portions of the region (Figures 2 a-b). In the southeastern AS, Argo shows weaker negative SSS anomalies of up to 0.5 psu during this time period. This region of negative SSS anomalies connects to the northernmost regions of the BoB, first along Sri Lanka and then up the east coast of India. In the northernmost sectors of the BoB, the SSS anomalies remain negative, but have much higher magnitudes. Some disagreement between Argo and Aquarius occurs over this region, with Aquarius showing a slight positive SSS anomaly in the northern BoB. In the eastern and southern portions of the BoB, positive SSS anomalies exist.

In July, the AS experiences little change in its northern and central regions (Figures 2 c-d), but is impacted by weak positive anomalies in its southeastern corner which persist into the Sri Lanka region (see SL box in Figure 1). Within the BoB, positive SSS anomalies exist throughout the region. A meridional gradient within the Bay shows maximum values of up to 1 psu to the north, which then

gradually approaches zero at the entrance of the Bay. The fact that the anomalies are positive within the BoB during the SWM requires some explanation as the highest rates of precipitation and river discharge for this region occur between June-September and the lowest in January-April (see Figure 1 of Akhil et al., 2014). We surmise that higher negative SSS anomalies may occur by October in the northern BoB, when the horizontal freshwater transport from the Ganges and Brahmaputra rivers reaches its maximum in the northern Bay. BoB box average Aquarius salinity in January is 33.41 psu and 32.85 psu in July, but the spatial anomalies show a suppressed freshwater plume at the northern sector of the Bay. The largest annual freshwater plume occurs in the northern BoB between August-October (see Figure 2 of Akhil et al., 2014). During January, however, the freshwater plume is at its annual minimum, but the monsoon season freshwater plume still circulates in the BoB through prevailing circulations. Akhil et al. (2014) also find that while surface freshwater flux and riverine input are high during the SWM, vertical advection of salty waters from the subsurface balances the salt budget and keeps the tendency term from becoming significantly lower than that of the remaining months of the year.

Figure 3 shows the seasonal SSS anomalies for HYCOM, SODA, ECCO2, CORA v3.4, and ECMWF. For January, all the products confirm low SSS anomalies in the northern and central portions of the AS (Figures 3 a, c, e, g, i). In the southeastern AS and Sri Lanka box region, all products account for the presence of the negative SSS anomalies, although their magnitudes differ, with HYCOM and CORA v3.4 producing the largest magnitudes. Disagreement between the datasets increases within the northern sector of the BoB, with HYCOM, SODA, ECCO2, ECMWF, and Aquarius profiles all showing the positive SSS anomaly. Both Argo and CORA v3.4 instead show negative salinity anomalies for this region.

In the AS during July, the models show minimal positive salinity anomalies (Figures 3 b, d, f, h, j) and disagree with the larger magnitudes produced by Aquarius (Figure 2c). In the Sri Lanka box, larger positive anomalies are present and again match with the Argo profile better than that of Aquarius. The increased salinity values present in the Sri Lanka box during this period are due to the advection of salty AS waters into the region along the SMC (Schott and McCreary, 2001; Vinayachandran et al., 2013). This effect is also observed in the western and southwestern portions of the BoB during the same period as salty AS waters enter the Bay and travel along the East Indian coast through the EICC (Shankar et al., 2002). HYCOM, SODA, and ECMWF appear to show greater spatial variability in the BoB than Aquarius, Argo, and CORA v3.4, which all show a swath of positive SSS anomalies across the

northernmost portion of the Bay. This effect is likely due to the relatively higher spatial resolutions that the model simulations provide, which show the highly heterogeneous nature of SSS in the BoB.

In general, differences between the observed and model simulated SSS anomaly fields are low although the Aquarius data tend to resemble the model solution more than the Argo floats data. This is due to the higher resolution provided by the satellite and allows the observation of finer salinity gradients that are not present in the lower resolution and highly smoothed Argo floats data. The products show the large-scale SSS features confirmed by the observations, but also elude to smaller scale SSS features especially in the BoB. Due to their relatively coarse spatial resolution the observations cannot yet confirm the accuracy of these features, but the products are likely resolving the highly variable nature of SSS within the Bay.

3.2 Surface Salt Transport Variability

Figure 4 shows mean zonal and meridional surface salt transports overlain with OSCAR currents for the three Januarys between August 2011 and May 2014 for both Aquarius and Argo. Zonal flow is westward throughout most of the NIO and contributes to the westward advection of salt along the NMC. The only other region of higher zonal surface salt transport is found within the SEC, which flows to the west year around (Figures 4a, 4c). Although lower in magnitude, the meridional surface salt transport has maxima within both the AS and BoB (Figures 4b, 4d). The salty AS waters are pushed northward by the western portion of the cyclonic feature off the Somali coastline and also by the currents within the region associated with the WICC. As Aquarius and Argo do not resolve salinity well along the coastlines, signature features such as the alongshore Somalia Current and the WICC are not well represented here.

Figure 5 shows the mean January surface salt transport for the models between 2008 and 2011 with the exception of SODA, which runs between 2008 and 2010. The models provide a very similar picture for this time period in the NIO, but they also allow closer examination of important coastal features that Aquarius and Argo cannot resolve. Within the AS, the zonal flow is weakly westward with northward meridional transports into the region. The WICC can now also be more clearly seen. In the BoB, the zonal surface transport is also to the west with northward meridional surface transport to the north across the region. Between the two northern seas, a strong zonal surface salt transport has set up along the NMC to the south of Sri Lanka. A strong northward meridional component is also present as the current turns into the AS. The Somali current can also now be clearly seen running southward at this time of

year. While CORA v3.4 and ECMWF resolve the cyclonic rotation pattern off the Somali coastline as observed in the OSCAR currents (Figure 4), the other models do not produce this feature and give more emphasis to the Somali current.

The Aquarius and Argo derived mean surface salt transports for the two Julys between August 2011 and May 2014 are shown in Figure 6. The AS is dominated by both an eastward zonal flow and southward meridional flow as salt is advected out of the region along the SMC. A slightly higher zonal signal appears to the far west of the AS, as salt emerges from the Somali current. In the BoB, the surface salt transport is much lower with only a very small eastward zonal component. Off the east coast of Africa, the surface salt transport is affected by the eastward flow north of the equator and westward flowing SEC south of the equator. Here again, the Somali current is underrepresented and cannot be seen due to OSCAR's inability to properly resolve its signal.

Figure 7 shows model mean July surface salt transport between 2008 and 2011 with the exception of SODA, which runs between 2008 and 2010. In the AS, the models show both strong zonal and meridional components. Salt is again seen advecting down the West Indian coast along the WICC, which eventually flows into the zonal SMC along Sri Lanka. In the BoB, zonal and meridional surface salt transports are weak. However, the HYCOM, SODA, and ECMWF simulations show positive and higher surface salt transport along the east coast of India. The higher meridional surface salt transport might be due to the coastal upwelling of saline waters during the SWM. Only SODA and ECMWF show a connected, coherent flow along the coastline, and the HYCOM and ECCO2 surface salt transports show a broken connection. Model agreement is higher than Figure 5 with the exception of SODA.

To summarize, surface salt transports calculated using the observed and modeled SSS fields produce the expected large-scale salt advection between the AS and BoB during both monsoon seasons. Although we showed in Section 3.1 that the SSS fields produced by both the observations and the model simulations are highly similar, the modeled products reveal more spatial variability during both January and July across the NIO. This is mostly due to the fact that OSCAR currents must be used to calculate the observed surface salt transport fields as neither Aquarius nor Argo have their own surface current products. The OSCAR currents prove to be too coarse in resolution and feature oversimplified dynamics (Johnson et al., 2007; Sikhakolli et al., 2013) both of which cause the surface salt transport fields for Aquarius and Argo to have lower magnitudes and a lack of spatial variability. That said, model disagreement can be large in localized regions of the NIO making it difficult to confirm smaller scale

features. Because the analyses products, with the exception of CORA v3.4, produce the large-scale features as well as enhanced spatial variability it is likely that their solutions are closer to the correct approximation.

3.3 Subsurface Salinity Variability

The salinity variability of the major sub-regions of the NIO is also seen in the depth profiles. Figure 8 shows the time-depth section of AS salinity for Argo, CORA v3.4, and all numerical models under consideration. The MLD and ILD are overlain on the plots. Argo is used as the observation in this section, but again it should be noted that all of the modeled products being used assimilate Argo into their analysis. The vertical gradient is approximately 1 psu between the surface and 200 m with the highest salinity at the surface. There is some model disagreement with respect to this vertical gradient. Low salinity water can be seen at the sea surface on a seasonal basis centered on the monsoon transition periods. Among the models, there is disagreement in the salinity magnitudes and the time of occurrences of high salinity. HYCOM (Figure 8b) shows the seasonal occurrence of the largest plume of low salinity waters in the upper 50 m layer, as compared to the Argo salinity. SODA and also CORA3.4 (Figures 8c, 8f) show relatively little decrease in salinity at the surface on a seasonal cycle. Finally, both the MLD and the ILD share the seasonality of the anomalous decrease in surface salinity during boreal spring. The models disagree on how deep each layer should be, but all products, excluding HYCOM (Figure 8b), show a decrease in the layer thickness in boreal spring and fall and an increase in layer depth during the peak of the NEM and SWM. Barrier layer thickness (BLT = ILD-MLD) exhibits strong seasonality, with larger thickness up to 25 m during each monsoon season and decreased thickness during monsoon transitions. Earlier studies have shown the importance of barrier layer dynamics in the AS, most notably the South Eastern Arabian Sea (SEAS) warm pool (Nyadjro et al., 2012). Recent satellite estimates of BLT (Felton et al., 2014) show a small annual mean BLT for the AS with a seasonal cycle and magnitudes similar to this present study.

Figure 9 shows the time-depth salinity structure for the BoB. A shallow lens of low salinity water occurs year around, but has the greatest magnitude during the NEM. All products have the lowest vertical depth of the freshwater lens up to 50 m with the exception of HYCOM which reaches slightly deeper to up to 75 m. HYCOM produces very low salinity waters and SODA produces relatively higher salinity waters, when compared to Argo salinity. Between the SWM and NEM transition, freshest water appears at the surface, and the mixed layer thickness is small. This adjustment in the thermocline brings

with it salty waters from deeper layers. The ECCO2 product does not resolve this phenomenon (Figure 9d). The BLT appears to have low seasonality in the products of HYCOM and ECCO2. Argo, CORA v3.4, ECMWF, and SODA show thicker (40 m) BLT. The studies of Felton et al. (2014) support the results of the model products' BLT, with the highest annual mean BLT in the northern BoB. The mixed layer of this region is often flush with low salinity waters due to its close proximity to large riverine output and lower rates of E-P (Sengupta et al., 2006). The positive buoyancy at the surface inhibits mixing of both colder and saltier waters from below. This process sets up a feedback mechanism that keeps the BoB surface waters continuously warm, which allows for more convection and in turn more precipitation. This transport of freshwater in the surface layer keeps the water column highly stable and thus perpetuates the cycle (Drushka et al., 2014). Although the mixed layer is at its most shallow in the annual cycle during this time, the ILD experiences a much greater increase in depth in comparison. This suggests that although the MLD is contributing to the increased BLT, the increase in ILD is the primary driver of annual BLT variability.

Figure 10 shows the time-depth salinity structure for the Sri Lanka box region. This region is especially important because it is the exchange zone between the AS and BoB. The most notable feature is the highly seasonal subsurface layer with respect to salinity. Around January, during the NEM, a layer of low salinity water appears at the surface with a penetration depth up to 50 m. This is caused by the BoB freshwater carried along the NMC. This is the predominant mode, but for a short period of time during the SWM, a salty signal appears at the surface as water from the AS travels along the SMC into the BoB. Vinayachandran et al. (2013) confirms a mean July SSS of 34.5 psu with a 35 psu isohaline between 50 and 100 m depth in this region. Here again, Argo, CORA v3.4, ECMWF, and SODA all generate maximum BLT values of up to 40 m, while HYCOM and ECCO2 produce only shallow BLTs of 10 m or less. Felton et al. (2014) found their own annual mean BLT estimate for this region to be between 15 and 30 m. Most likely barrier layer dynamics mirror those found in the BoB, as the region is also flush with warm and fresh surface water on the same seasonal time scales. A unique event in this time series occurred in the Argo profile during November-December 2011. A stronger salinity core occurs at 75 m depth after only a brief influx of higher surface salinities during August-September. During the same period of time when the maximum core reaches its greatest intensity of salinity, exceeding 35.5 psu, a deep ILD layer forms under the influence of strong freshwater flux at the surface. It appears that the formation of a barrier layer prevented mixing that typically causes the core maximum to fade into the background salinity profile. This deep barrier layer allowed the core maximum to reach a

higher salinity than in other years and to persist several months longer than the preceding 3 seasonal cycles. The only other model that effectively resolves this event is the ECMWF (Figure 10e). Not surprisingly, the ECMWF barrier layer is also quite deep during this time period. As the ECMWF assimilates Argo data it is difficult to ascertain if the ECMWF is correctly reproducing the feature or is relying heavily on the Argo analysis to produce its own. CORA v3.4, ECCO2, and SODA also resolve an anomalous deep barrier layer, but fail to produce the core salinity maximum and the deep barrier layer with the correct magnitude and duration. HYCOM fails to capture both the increased BLT and the core maximum.

Generally the model solutions compare well with the Argo analysis, but it can be difficult to make direct comparisons when Argo is assimilated into each product. In general, ECMWF appears to agree with the Argo analysis most closely, but this may be more of an indication of how much the product relies on the Argo dataset to generate its own analysis than how accurate the product itself is. CORA v3.4, ECCO2, and SODA are also similar to the Argo analysis, but it is more obvious that they are generating their own independent solutions instead of just reproducing the Argo analysis. HYCOM produces the greatest discrepancies across all three regions when compared to both Argo and the other product solutions. In all three regions there appears to be a low salinity bias in the HYCOM analysis likely due to a difference in surface forcing. The salty and fresher signatures in each region also reach deeper into the water column in the HYCOM solution, which may be a result of its more flexible vertical coordinate system. It is worth mentioning that the sources and quality control checks of assimilated data such as Argo data vary among the laboratories that run the different models and could be a source of the discrepancies.

3.4 Depth-Integrated Salt Transport Variability

We computed depth-integrated salt transports in order to understand the advective processes throughout the entire water column. Transports within the AS are shown in Figure 11a. The time series data show strong seasonality for all transports with a maximum southward transport in January and a maximum northward transport in July. Analysis of the four-year mean transports along the lines of longitude in the basin (Figure 11b) shows larger transports off the Somali coast (49-52°E). The Somali current flows southward in January and northward in July, and explains the seasonality of the transports across the southernmost portion of the basin. Net depth-integrated salt transports are -84×10^6 kg s^{-1} in January and 37×10^6 kg s^{-1} in July. Salt lost during the NEM takes approximately an entire monsoon

season to be replaced during the SWM. It should be noted that ECCO2, ECMWF, and SODA closely track each other in magnitude throughout the entire time series, but HYCOM produce different estimates with erratic jumps and dips in magnitude not apparent in the other model outputs. The difference in magnitude seen in the HYCOM profile can be explained by larger subsurface transport estimates. Figure 12 shows monthly mean time-depth salt transports across the 6°N latitudinal boundary of the AS. The reanalysis products produce similar estimates in both the surface and subsurface, but HYCOM has larger transport estimates at greater depths. Another interesting feature is that these depth profiles appear to contradict the seasonal profile seen in the absolute transports in Figure 11a. The surface currents are in phase with the NMC and SWM currents, whereas the net depth-integrated transports are in line with the seasonality of the Somali current. If the profiles in Figure 12 are integrated for all depths, the sign and magnitude of these transports agree with those found in Figure 11a. This result suggests that at this western boundary, the surface currents are dominated by the seasonality of the monsoons, but when the subsurface currents are integrated as well they overwhelm the surface advection contribution (Figure 12). This is an important result and in this region one should not assume that the total salt transports can be described by the surface advection alone.

In the BoB, northward maximum depth-integrated salt transport occurs in January and southward maximum occurs in July (Figures 11c). Net depth-integrated salt transports are approximately 51×10^6 kg s^{-1} in January and -58×10^6 kg s^{-1} in July. The January and July estimates are out of phase with the local surface monsoon currents, but Figures 5 and 7 suggest an explanation. At the surface during both months the correct monsoon coastal current can be seen near Sri Lanka and on the eastern coast of India. On the eastern side of the 6°N boundary the sign of the surface salt transport is opposite to that of the western side. Integrating across all lines of longitude causes the sign to reverse when compared to the monsoon coastal current. An analysis of the mean meridional transports across the BoB at 6°N (Figure 11d) shows maximum southward salt transports centered on 82°E and maximum northward transports centered on 84°E. These spatial maxima are caused by the local cyclonic eddy that forms off the eastern coast of Sri Lanka during the SWM (Vinayachandran et al., 1999). The surface monsoon current is observed near 94°E. Shankar et al. (2002) show the turning of the SMC from eastward to northeastward at approximately the same location (see their Figure 2). The two flow patterns present at 82°E and 84°E explain the seasonality of the BoB transports at 6°N, and overshadow the magnitude of the SMC at this latitudinal band of the basin. The seasonality of the BoB is not as smooth as the pattern found within the AS and it is difficult to ascertain a time period over which the meridional transports come to

equilibrium. ECMWF compares least favorably, with erratic seasonal behavior and larger magnitudes. Low overall model agreement suggests that the models perform poorly in general within this region, leaving an inaccurate interpretation of transports for this location. Model agreement is much higher in space, although ECCO2 misses the influence of the SMC at 94°E (Figures 11d). Figure 13 shows monthly mean time-depth salt transports across the 6°N section of the BoB. Again the reanalysis products compare most favorably, but here HYCOM is more similar to the reanalysis products. Unlike the AS, the subsurface transports have less effect on the sign of the total transports as the seasonality of the surface advection agrees with that of the total transport estimates in Figure 11c.

Perhaps unsurprisingly, the three reanalyses products compare most favorably with respect to the transport estimates. Time-depth contours of salt transports for both regions (Figure 12 and Figure 13) demonstrate this fact. The spikes seen in the HYCOM estimates for the AS are caused primarily by subsurface transports that are higher in magnitude when compared to the reanalysis estimates (Figure 12). It is difficult to say whether this is an artifact or the true signal, but discrepancies between reanalyses products and true model simulations can be expected. Although there are small differences, HYCOM compares better to the reanalyses estimates in the BoB. Further, surface transports for all four products in both regions agree quite well in both time and space. Our results suggest that when estimating total transports across the 6°N section of the AS it is important to include subsurface advection, as any quantitative analysis done without it will produce the incorrect sign and magnitude. This issue is not as relevant in the BoB analysis and the sign of the surface transports is typically the same as that of the total estimate. Overall, while difficult to validate, these transports provide a sufficient baseline estimate for total water column advection into and out of each basin at 6°N on a seasonal basis and future research is required to ascertain the true transports to compare with these model estimates.

4. Summary and Conclusions

The present study shows the salinity of the NIO to be highly variable in both time and space. Aquarius does a good job of estimating seasonal surface salinity for this region. The Aquarius seasonal SSS anomaly fields show that the satellite allows the observation of finer salinity gradients than possible in the Argo floats data. Aquarius opens up new possibilities for the observation of the NIO by revealing spatial variability that was previously only available in simulated data. That said, due to radio frequency interference near the coast and Argo’s inability to take measurement in these regions, model simulations are still necessary when studying salinity advection within the important coastal currents in both the AS

and BoB. Calculating surface salinity advection during each monsoon season using Aquarius and Argo is possible due to their high degree of salinity accuracy, but OSCAR generates advective terms that are smaller in magnitude and much lower in resolution when compared to the simulated data. Our results suggest that when using these observational datasets to study surface salinity advection, a more robust current analysis should be used instead of the oversimplified OSCAR solution.

In the time-depth profiles, the effects of the seasonal monsoons can clearly be seen. With respect to salinity, the AS is the most static of the three regions, but does experience high surface variability during the NEM when fresh BoB water is advected into the region. This is the time when formation of a barrier layer is most favorable, but our box is too far away from the SEAS region to see a larger seasonal barrier layer. The BoB is much more variable and experiences barrier layer formation much more regularly. Our results show barrier layer depth maxima during boreal winter as the isothermal layer deepens, not when the mixed layer is at a minimum during the SWM. The Sri Lanka region more closely resembles the BoB, but the impact of freshwater is not as large and is much more seasonal. We observed a strong interannual anomaly in the region in the latter part of 2010. A peak in horizontal surface freshwater advection into the region caused a deep barrier layer to form and generated positive subsurface salinity anomalies. This suggests that barrier layer formation is important for the region, but is largely a function of the magnitude of the freshwater plume coming from the BoB and is highly variable from year to year.

The approximate net depth-integrated meridional salt transports for the AS are -84×10^6 kg s^{-1} in January and 37×10^6 kg s^{-1} in July. In the BoB, the estimates are 51×10^6 kg s^{-1} in January and -58×10^6 kg s^{-1} in July. The Somali current dominates the total depth-integrated salt transport profile in the AS, although at the surface the SMC and NMC drive the advective forces. In the BoB, the depth-integrated transports are out of phase with the local surface monsoon currents. In January and July, although the correct surface monsoon currents are present to the west near Sri Lanka, surface salt transports in the central and eastern BoB at 6°N are opposite that of the EICC (Figures 5 and 7) and cause the sign of the total integrated transports across the boundary to be out of phase with the large-scale, seasonal monsoons currents. Also, the local cyclonic eddy that forms during the SWM causes the large southward and northward spikes in the mean longitudinal distribution of depth-integrated salt transports on the western side of the boundary.

Several model simulations were examined and each model's performance is quite variable depending on the specific location and calculation performed. All models produce seasonal SSS values

that match with that of both Aquarius and Argo quite closely although there are some differences across the spatial domain. At depth, model disagreement becomes more troublesome. HYCOM (v2.2.19) appears to have a fresh bias near the surface likely due to a difference in its internal surface forcing. ECMWF performs better when compared to Argo by correctly producing anomalous subsurface salinity core structures associated with barrier layer formation in the Sri Lanka box, but it is unclear if this is due to its overall accuracy or the possibility that it relies heavily on the Argo analysis in its assimilation process. CORA v3.4, ECCO2, and SODA capture the general structure of each sub-region quite well, but do not correctly produce the anomalous event in the Sri Lanka box. With respect to depth-integrated salt transports, all four products capture a very similar mean spatial structure at all lines of longitude along 6°N, but disagree on the magnitude and seasonality. HYCOM shows the largest disparity by creating large spikes in magnitude across the time series even though the general seasonal trend is present in the AS. In the BoB, all four products disagree on the seasonality within the time series, but ECMWF creates spikes similar to the HYCOM data in the AS. Though the data and model products used in this study provide useful qualitative and quantitative information, many more questions than answers are raised. Aquarius is able to provide highly accurate SSS measurements quickly to the scientific community, but a much clearer perspective of global, seasonal, and eventually interannual variations in the SSS variable is essential. Argo has been a great step forward for understanding the global ocean salinity structure with depth, but remains an imperfect solution. Float density is still relatively low, leaving out under sampled regions such as the BoB. Also, the nature of Lagrangian data collection does not allow for the continuous analysis of areas such as the southern and eastern Sri Lanka box region, the two regions we have shown to be important as seasonal exchange zones. Their depth range is also too low to calculate transports, and we must rely on model and reanalysis data that we have little ability to verify. New and targeted data collection within the NIO must be deployed to confirm that model and reanalysis products are correctly representing this highly variable region. We hope that the estimations presented in this paper will guide other researchers towards gathering valuable *in situ* observations for this important yet under analyzed portion of the global ocean.

Acknowledgments

This work is supported by the ONR Physical Oceanography Program Award #N00014-12-1-0454 awarded to BS. One of the authors, VSNM, is thankful to the Director of the CSIR-NIO for his keen interest in the joint-collaborative research with BS at the University of South Carolina, Columbia, USA. The authors would like to thank the editor and two anonymous reviewers for their constructive

comments and suggestions that greatly improved the manuscript. Aquarius version 3.0 data was provided by NASA/JPL PO. DAAC. The HYCOM model simulations were provided by Jay F. Shriver, Naval Research Laboratory, Stennis Space Center, Mississippi. Monthly gridded Argo temperature and salinity profiles were obtained from the Asia Pacific Data-Research Center (APDRC) of the International Pacific Research Centre (IPRC). The state estimates were provided by the ECCO Consortium for Estimating the Circulation and Climate of the Ocean funded by the National Oceanographic Partnership Program (NOPP). ECCO2 outputs were obtained from NASA/JPL (ftp://ecco2.jpl.nasa.gov). ORAS4 outputs were obtained from ftp://ftp.icdc.zmaw.de/EASYInit/ORA-S4/monthly_1x1/. SODA reanalysis outputs were obtained from http://dsrs.atmos.umd.edu/DATA/soda_2.2.4/. CORA v3.4 outputs were obtained from the Coriolis Data Center (http://www.coriolis.eu.org/Science/Data-and-Products/CORA v3.4). OSCAR outputs were obtained from http://podaac.jpl.nasa.gov made freely available by the OSCAR Project Office. Indian Ocean bathymetry data were obtained from http://www.nio.org/?option=com_subcategory&task=show&title=Sea-floor+Data&tid=2&sid=18&thid=113. This has the NIO contribution number XXXX.

Reference:

Akhil, V. P., F. Durand, M. Lengaigne, J. Vialard, M. G. Keerthi, V. V. Gopalakrishna, C.

Deltel, F. Papa, and C. de Boyer Montégut, 2014: A modeling study of the processes of surface salinity seasonal cycle in the Bay of Bengal. *J. Geophys. Res. Oceans*, **119**, doi: 10.1002/2013JC009632.

Balmaseda, M. A., K. Mogensen, and A. Weaver, 2013: Evaluation of the ECMWF Ocean Reanalysis ORAS4, *Q. J. R. Meteorol. Soc*., **139**, 1132-1161, doi: 10.1002/qj.2063

Bonjean, F., and G. S. E. Lagerloef, 2002: Diagnostic model and analysis of surface currents in the tropical Pacific Ocean. *J. Phys. Oceanogr*., **32**, 2938-2954.

Cabanes C., A. Grouazel1, K. von Schuckmann, M. Hamon, V. Turpin, C. Coatanoan, F. Paris, S. Guinehut, C. Boone, N. Ferry, C. de Boyer Montegut, T. Carval, G. Reverdin, S. Pouliquen, and P.-Y. Le Traon, 2013: The CORA dataset: validation and diagnostics of in-situ ocean temperature and salinity measurements. *Ocean Science*, **9(1)**, 1-18.

Carton, J. A., and B. S. Giese, 2008: A reanalysis of ocean climate using Simple Ocean Data Assimilation (SODA). *Mon. Wea. Rev*., **136**, 2999–3017, doi:10.1175/2007MWR1978.1.

Chassignet, E. P., L. T. Smith, G. R. Halliwell, and R. Bleck, 2003: North Atlantic Simulations with the Hybrid Coordinate Ocean Model (HYCOM): Impact of the Vertical Coordinate Choice, Reference Pressure, and Thermobaricity. *J. Phys. Oceanogr.*, **33**, 2504–2526.

de Boyer Montégut, C., G. Madec, A. S. Fischer, A. Lazar, and D. Iudicone, 2004: Mixed layer depth over the global ocean: An examination of profile data and a profile-based climatology. *J. Geophys. Res.*, **109**, C12003, doi: 10.1029/2004JC002378.

Dee, D. P., et al., 2011: The ERA-Interim reanalysis: Configuration and performance of the data assimilation system. *Q. J. R. Meteorol. Soc*., **137**, 553–597, doi:10.1002/qj.828.

Dohan, K., and N. Maximenko, 2010: Monitoring ocean currents with satellite sensors. *Oceanography*, **23 (4)**, 94-103, doi:10.5670/oceanog.2010.08.

Felton, C. S., B. Subrahmanyam, V. S. N. Murty, and J. F. Shriver, 2014: Estimation of the barrier layer thickness in the Indian Ocean using Aquarius Salinity. *J. Geophys. Res Oceans.*, **119**, doi: 10.1002/2013JC009759.

Findlater, J., 1969: A major low-level air current near the Indian Ocean during the northern summer. *Q. J. R. Meteorol. Soc.*, **95**, 362-380, doi: 10.1002/qj.4970954409.

Gemmell, A. L., G. Smith, K. Haines, and J. D. Blower, 2008: Evaluation of water masses in ocean synthesis products. *CLIVAR-Exchanges*, **13 (47)**, 7–9.

Hamon, M., G. Reverdin and P.-Y. Le Traon, 2012: Empirical correction of XBT data. *J. Atmos. Oceanic. Technol*., **29**, 960-973, doi: 10.1175/JTECH-D-11-00129.1.

Han, W., and J. P. McCreary Jr., 2001: Modeling salinity distributions in the Indian Ocean. *J. Geophys. Res.*, **106 (C1)**, 859-877, doi: 10.1029/2000JC000316.

Hanawa, K., P. Rual, R. Bailey, A. Syc, and M. Szabados, 1995: A new depth-time equation for Sippican or TSK T-7, T-6 and T-4 expendable bathythermographs (XBT). *Deep Sea Res. I*, **42**, 1423–1451.

Jensen, T. G., 2001: Arabian Sea and Bay of Bengal exchange of salt and tracers in an ocean model. *Geophys. Res. Lett.*, **28**, 3967-3970.

Jensen, T. G., 2003: Cross-equatorial pathways of salt and tracers from the northern Indian Ocean: Modeling results. *Deep-Sea Res. II*, **50**, 2111-2127.

Johnson, E., F. Bonjean, G. S. E. Lagerloef, and J. T. Gunn, 2007: Validation and Error Analysis of OSCAR Sea Surface Currents. *J. Atmos. Oceanic Technol.*, **24**, 688-701.

Lagerloef, G., F. R. Colomb, D. Le Vine, F. Wentz, S. Yueh, C. Ruf, J. Lilly, J. Gunn, Y. Chao, A. deCharon, G. Feldman, and C. Swift, 2008: The Aquarius/SAC-D mission: designed to meet the salinity remote-sensing challenge. *Oceanography*, **21 (1)**, 68-81.

Lebedev, K. V., H. Yoshinari, N. A. Maximenko, and P. W. Hacker, 2007: YoMaHa'07: Velocity data assessed from trajectories of Argo floats at parking level and at the sea surface. *IPRC Technical Note*, **4(2).**

Lee, T., T. Awaji, M.A. Balmaseda, E. Greiner, and D. Stammer, 2009: Ocean state estimation for climate research. *Oceanography*, **22 (3)**, 160–167.

Masson, S., et al. (2005), Impact of barrier layer on winter-spring variability of the southeastern Arabian Sea. *Geophys. Res. Lett.*, **32**, L07703, doi: 10.1029/2004GL021980.

McCreary, J. P., P. K. Kundu, and R. L. Molinari, 1993: A numerical investigation of dynamics, thermodynamics and mixed-layer processes in the Indian Ocean. *Prog. Oceanogr.*, **31**, 181-244.

Menemenlis, D., J. Campin, P. Heimbach, C. Hill, T. Lee, A. Nguyen, M. Schodlock, and H. Zhang, 2008: ECCO2: High resolution global ocean and sea ice data synthesis. *Mercator Ocean Quarterly Newsletter*, **31**, Mercator Ocean, Ramonville Saint-Agne, France, 13–21.

Metzger, E. J., O. M. Smedstad, P. G. Thoppil, H. E. Hurlburt, J. A. Cummings, A. J. Wallcraft, L. Zamudio, D. S. Franklin, P. G. Posey, M. W. Phelps, P. J. Hogan, F. L. Bub, and C. J. DeHaan, 2014: US Navy operational global ocean and Arctic ice prediction systems. *Oceanography*, **27(3)**, 32-43.

Munoz, E., B. Kirtman, and W. Weijer, 2011: Varied representation of the Atlantic Meridional Overturning across multidecadal ocean reanalyses. *Deep Sea Res. Part II*, **58**, 1848-1857.

Murty, V. S. N., Y. V. B. Sarma, D. P. Rao, and C. S. Murty, 1992: Water characteristics, mixing and circulation in the Bay of Bengal during southwest monsoon. *J. Mar. Res.*, **50**, 2, 207-228.

Nihashi, S., K. I. Ohshima, and N. Kimura, 2012: Creation of a heat and salt flux dataset associated with sea ice production and melting in the Sea of Okhotsk. *J. Climate*, **25**, 2261-2278.

Nyadjro, E. S., B. Subrahmanyam, and J. F. Shriver, 2011: Seasonal variability of salt transport during the Indian Ocean monsoons. *J. Geophys. Res.*, **116**, C08036, doi: 10.1029/2011JC006993.

Nyadjro, E. S., B. Subrahmanyam, V. S. N. Murty, and J. F. Shriver, 2012: The role of salinity on the dynamics of the Arabian Sea mini warm pool. *J. Geophys. Res.*, **117**, C09002, doi: 10.1029/2012JC007978.

Nyadjro, E. S., B. Subrahmanyam, and B. S. Giese, 2013: Variability of salt flux in the Indian Ocean during 1960-2008. *Remote Sens. Environ.*, **134**, 175-193, doi: 10.1016/j.rse.201303.005.

Prasannakumar, S., and T. G. Prasad, 1996: Winter cooling in the northern Arabian Sea. *JGOFS (India)*, **71**, 834-841.

Rao, R. R., and R. Sivakumar, 2003: Seasonal variability of sea surface salinity and salt budget of the mixed layer of the north Indian Ocean. *J. Geophys. Res.*, **108(CI)**, 3009, doi: 10.1029/2001JC000907.

Sastry, J. S., D. P. Rao, V. S. N. Murty, Y. V. B. Sarma, A. Suryanarayana, and M. T. Babu, 1985: Watermass structure in the Bay of Bengal. *Mahasagar-Bull. Natl. Inst. Oceanogr.*, **18 (2)**, 153-162.

Schiller, A., S. E. Wijffels, and G. A. Meyers, 2004: Design requirements for an Argo float array in the Indian Ocean inferred from observing system simulation experiments. *J. Atmos. Oceanic Technol.,* **21**, 1598-1620.

Schott, F. A., J. Reppin, J. Fischer, and D. Quadfasel, 1994: Currents and transports of the Monsoon Current south of Sri Lanka. *J. Geophys. Res.,* **99**, 25,127-25,141.

Schott, F. A., and J. P. McCreary, 2001: The monsoon circulation of the Indian Ocean. *Prog. Oceanogr.,* **51**, 1-123.

Sengupta, D., G. N. Bharath Raj, and S. S. C. Shenoi, 2006: Surface fresh-water from Bay of Bengal runoff and Indonesian Throughflow in the tropical Indian Ocean. *Geophys. Res. Lett.,* **33**, L22609, doi: 10.1029/2006GL027573.

Sengupta, D., B. R. Goddalehundi, and D. S. Anitha (2008), Cyclone-induced mixing does not cool SST in the post-monsoon north Bay of Bengal, *Atmos. Sci. Lett.,* **9**, 1-6, doi: 10.1002/asl.162.

Shankar, D., P. N. Vinayachandran, and A. S. Unnikrishnan, 2002: The monsoon currents in the north Indian Ocean. *Prog. Oceanogr.*, **52**, 63-120.

Sikhakolli, R., R. Sharma, S. Basu, B. S. Gohil, A. Sarkar, and K. V. S. R. Prasad, 2013: Evaluation of OSCAR ocean surface current product in the tropical Indian Ocean using in situ data. *J. Earth Syst. Sci*., **122**, 187–199.

Shetye, S. R., A. D. Gouveia, S. S. C. Shenoi, G. S. Michael, D. Sundar, A. M. Almeida, and K. Santanam, 1991: The coastal current of Western Indian during the Northeast monsoon. *Deep-Sea Res. Part A. Oceanographic Research Papers*, **38 (12)**, 1517-1529.

Shetye, S. R., A. D. Gouveia, D. Shankar, S. S. C. Shenoi, P. N. Vinaychandran, D. Sundar, G. S. Michael, and G. Nampoothiri, 1996: Hydrography and circulation in the western Bay of Bengal during the northeast monsoon. *J. Geophys. Res.,* **101**, 14,011-14,025.

Vinayachandran, P. N., Y. Masumoto, T. Mikawa, and T. Yamagata, 1999: Intrusion of the Southwest Monsoon Current into the Bay of Bengal. *J. Geophys. Res.,* **104**, 11,077-11,085.

Vinayachandran, P. N., and R. S. Nanjundiah, 2009: Indian Ocean sea surface salinity variations in a coupled model. *Clim. Dyn.,* **33**, 245-263.

Vinayachandran, P. N., D. Shankar, S. Vernekar, K. K. Sandeep, P. Amol, C. P. Neema, and A. Chatterjee, 2013: A summer monsoon pump to keep the Bay of Bengal salty. *Geophys. Res. Lett.,* **40**, 1777-1782, doi: 10.1002/grl.50274.

Wijffels S, J. Willis, C. M. Domingues, P. Barker, N. J. White, A. Gronell, K. Ridgway, and J. A. Church, 2009: Changing expendable bathythermograph fall rates and their impact on estimates of thermosteric sea level rise. *J. Clim.,* **21**, 5657–5672.

Wyrtki, K., *Oceanographic Atlas of the International Indian Ocean Expedition*, 531 pp., National Science Foundation, Washington, D. C., 1971.

Figure Caption List

Figure 1. Mean Indian Ocean depth (m, shaded) and mean Aquarius level 3 SSS between August 2011 and May 2014 (contoured). The boxes denote regions that are examined throughout the paper where AS is the Arabian Sea (60-70°E, 10-20°N), BoB is the Bay of Bengal (83-93°E, 12-18°N), and SL is Sri Lanka (75-85°E, 2-10°N). Dashed, black line along 6°N covering both the AS and BoB shows the latitudinal boundaries over which we calculated depth-integrated salt transports.

Figure 2. January (top row) and July (bottom row) SSS anomalies from both Aquarius level 3 data (left panel) and Argo floats (right panel) data averaged between August 2011 and May 2014. Anomalies were derived by subtracting the annual mean from the mean January and July spatial fields for each data set.

Figure 3. Mean January (left panel) and July (right panel) SSS anomalies for HYCOM (a-b), SODA (c-d), ECCO2 (e-f), CORA v3.4 (g-h), and ECMWF (i-j) averaged between January 2008 and December 2011, except SODA which only extends out to December 2010. Anomalies were derived by subtracting the annual mean from the mean January and July spatial fields for each data set.

Figure 4. Mean zonal (left panel) and meridional (right panel) surface salt transports for Aquarius (top row) and Argo (bottom row) for the three Januarys between August 2011 and May 2014. Mean OSCAR currents over the same time period have been overlain to show the flow patterns. All values are in kg m^{-2} s^{-1}. Note the different color scales for zonal and meridional surface salt transports.

Figure 5. Mean January zonal (left panel) and meridional (right panel) surface salt transports between 2008 and 2011 for HYCOM (a-b), SODA (c-d), ECCO2 (e-f), CORA v3.4 (g-h), and ECMWF (i-j) and between 2008 and 2010 for SODA. Mean January model derived surface currents for the same time period have been overlain to show the flow pattern with the exception of CORA v3.4, which uses OSCAR currents instead. All values are in kg m^{-2} s^{-1}. Note the different color scales for zonal and meridional surface salt transports.

Figure 6. Mean zonal (left panel) and meridional (right panel) surface salt transports for Aquarius (top row) and Argo (bottom row) for the two Julys between August 2011 and May 2014. Mean OSCAR currents over the same time period have been overlain to show the flow patterns. All values are in kg m^{-2} s^{-1}. Note the different color scales for zonal and meridional surface salt transports.

Figure 7. Mean July zonal (left panel) and meridional (right panel) surface salt transports between 2008 and 2011 for HYCOM (a-b), SODA (c-d), ECCO2 (e-f), CORA v3.4 (g-h), and ECMWF (i-j) and

between 2008 and 2010 for SODA. Mean July model derived surface currents for the same time period have been overlain to show the flow pattern with the exception of CORA v3.4, which uses OSCAR currents instead. All values are in kg m^{-2} s^{-1}. Note the different color scales for zonal and surface meridional salt transports.

Figure 8. Time-depth sections of box-averaged salinity, mixed layer depth (m, black line), and isothermal layer depth (m, white dashed line) in the Arabian Sea between January 2008 and December 2011 from Argo (a), HYCOM (b), CORA v3.4 (c), ECCO2 (d), ECMWF (e), and SODA (f).

Figure 9. Time-depth sections of box-averaged salinity, mixed layer depth (m, black line), and isothermal layer depth (m, white dashed line) in the Bay of Bengal between January 2008 and December 2011 from Argo (a), HYCOM (b), CORA v3.4 (c), ECCO2 (d), ECMWF (e), and SODA (f).

Figure 10. Time-depth sections of box-averaged salinity, mixed layer depth (m, black line), and isothermal layer depth (m, white dashed line) in the Sri Lanka box between January 2008 and December 2011 from Argo (a), HYCOM (b), CORA v3.4 (c), ECCO2 (d), ECMWF (e), and SODA (f).

Figure 11. Monthly time-series of depth-integrated salt transports across a 6°N section in the Arabian Sea (a) and Bay of Bengal (c) between 2008 and 2011 along with depth-integrated salt transports across all lines of longitude in the Arabian Sea (b) and the Bay of Bengal (d) averaged over all months between 2008 and 2011. Salt transports are in units of $\times 10^6$ kg s^{-1}.

Figure 12. Depth-time plot of monthly mean salt transport per unit depth ($\times 10^6$ kg s^{-1} m^{-1}) across 6°N in the Arabian Sea over the top 200 m (a-d) and over the entire water column (e-h).

Figure 13. Depth-time plot of monthly mean salt transport per unit depth ($\times 10^6$ kg s^{-1} m^{-1}) across 6°N in the Bay of Bengal over the top 200 m (a-d) and over the entire water column (e-h).

Table 1. Summary of the characteristics of model outputs used in this study

Product	ECCO2	HYCOM	ORAS4	SODA
Version	Cube 78	2.2.19	System 4	2.2.4
Model	Massachusetts Institute of Technology (MIT) General Circulation Model (MITgcm)	Miami Isopycnic Coordinate Ocean Model	Nucleus for European Modeling of the Ocean version 3 (NEMO3)	Parallel Ocean Program version 2 (POP2)
Horizontal resolution	18 km ×18 km	0.08°×0.08°	1°×1° with equatorial refinement (0.3°)	0.25°×0.4° (average)
Vertical levels	50	32	42	40
Assimilation method	Green's function optimization	NCODA 3DVAR with MODAS synthetics	Multivariate optical interpolation (OI)	OI
Data assimilated	Altimetry, Temperature (T) and Salinity (S) profiles from XBT, CTD, Argo, in-situ sea ice concentration	Altimetry, satellite SST and SSS, in situ Temperature (T) and Salinity (S) profiles from XBT, Argo, and moored buoys	Altimetry, T from XBT, T and S from CTD, Argo, and moorings	Altimetry, satellite and in-situ SST, T & S profiles from MBT, XBT, CTD, Argo, TAO and other buoys
Surface forcing	Weighted mean of satellite-derived wind products, NCEP/NCAR and ERA-40 reanalysis	Navy Operational Global Atmospheric Prediction System (NOGAPS) winds, heat fluxes and precipitation	ERA-Interim reanalysis and ECMWF operational archive	20CRv2 Ensemble Mean
Laboratory	National Aeronautics and Space Administration (NASA)	Naval Research Laboratory (NRL)	European Centre for Medium-Range Weather Forecasts (ECMWF)	Texas A&M University and University of Maryland
Data download	ftp://ecco2.jpl.nasa.gov/data1/cube/cube92/lat_lon/quart_90S_90N/	http://hycom.org/dataserver/glb-analysis	ftp://ftp.icdc.zmaw.de/EASYInit/ORA-S4/monthly_1x1/	http://dsrs.atmos.umd.edu/DATA/soda_2.2.4/
References	Menemenlis et al. 2008	Chassignet et al. 2003; Metzger et al., 2014	Balmaseda et al. 2013	Carton and Giese 2008

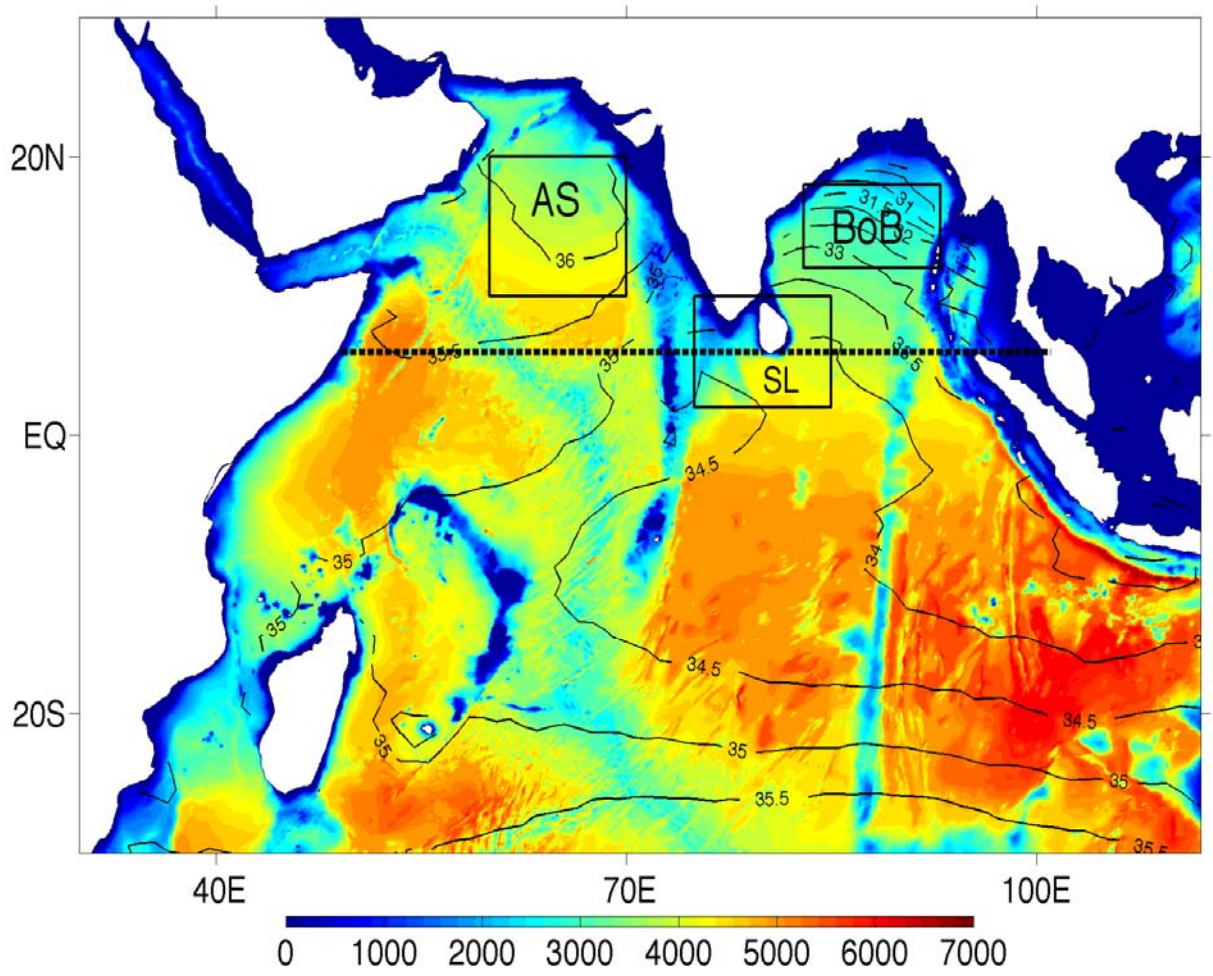

Figure 1. Mean Indian Ocean depth (m, shaded) and mean Aquarius level 3 SSS between August 2011 and May 2014 (contoured). The boxes denote regions that are examined throughout the paper where AS is the Arabian Sea (60-70°E, 10-20°N), BoB is the Bay of Bengal (83-93°E, 12-18°N), and SL is Sri Lanka (75-85°E, 2-10°N). Dashed, black line along 6°N covering both the AS and BoB shows the latitudinal boundaries over which we calculated depth-integrated salt transports.

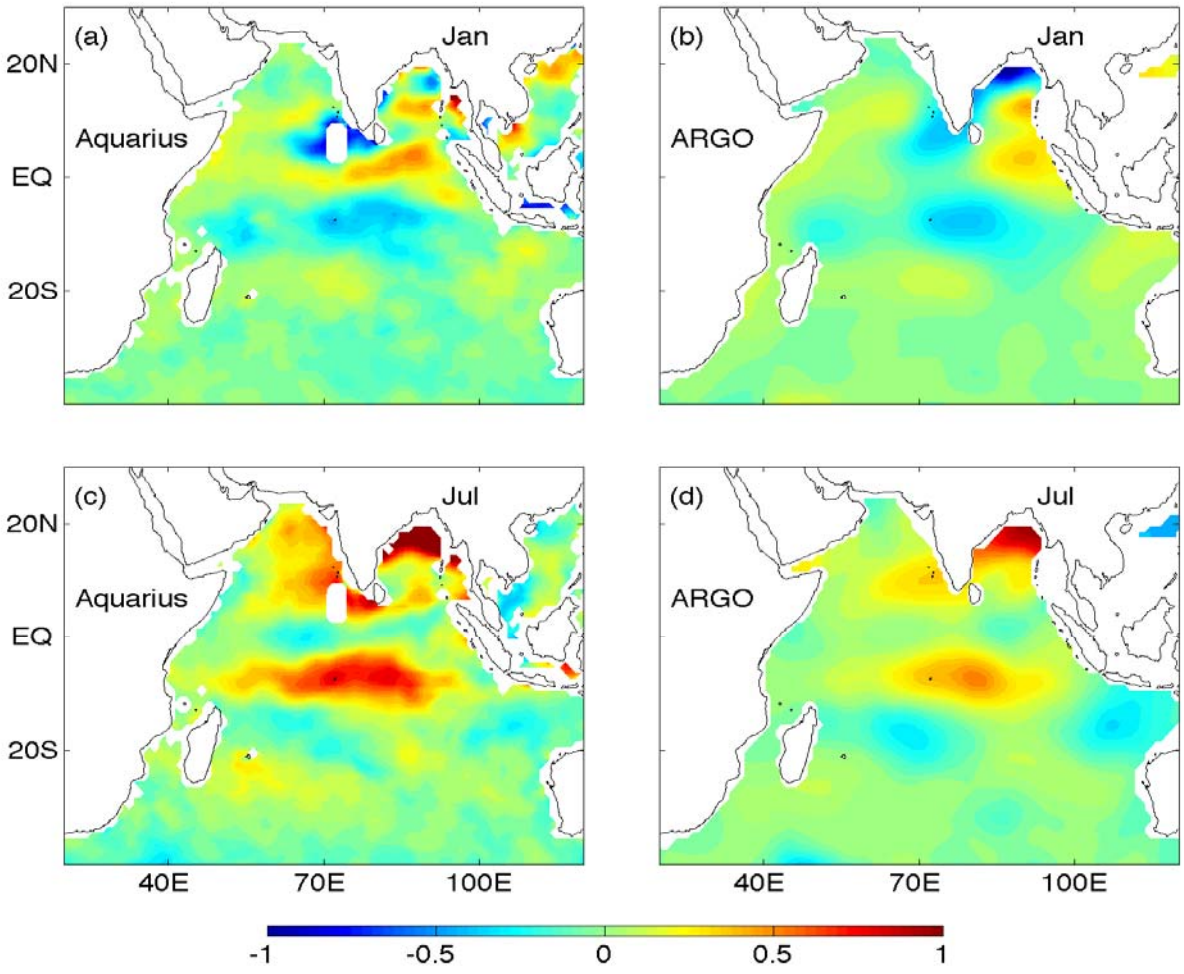

Figure 2. January (top row) and July (bottom row) SSS anomalies from both Aquarius level 3 data (left panel) and Argo floats (right panel) data averaged between August 2011 and May 2014. Anomalies were derived by subtracting the annual mean from the mean January and July spatial fields for each data set.

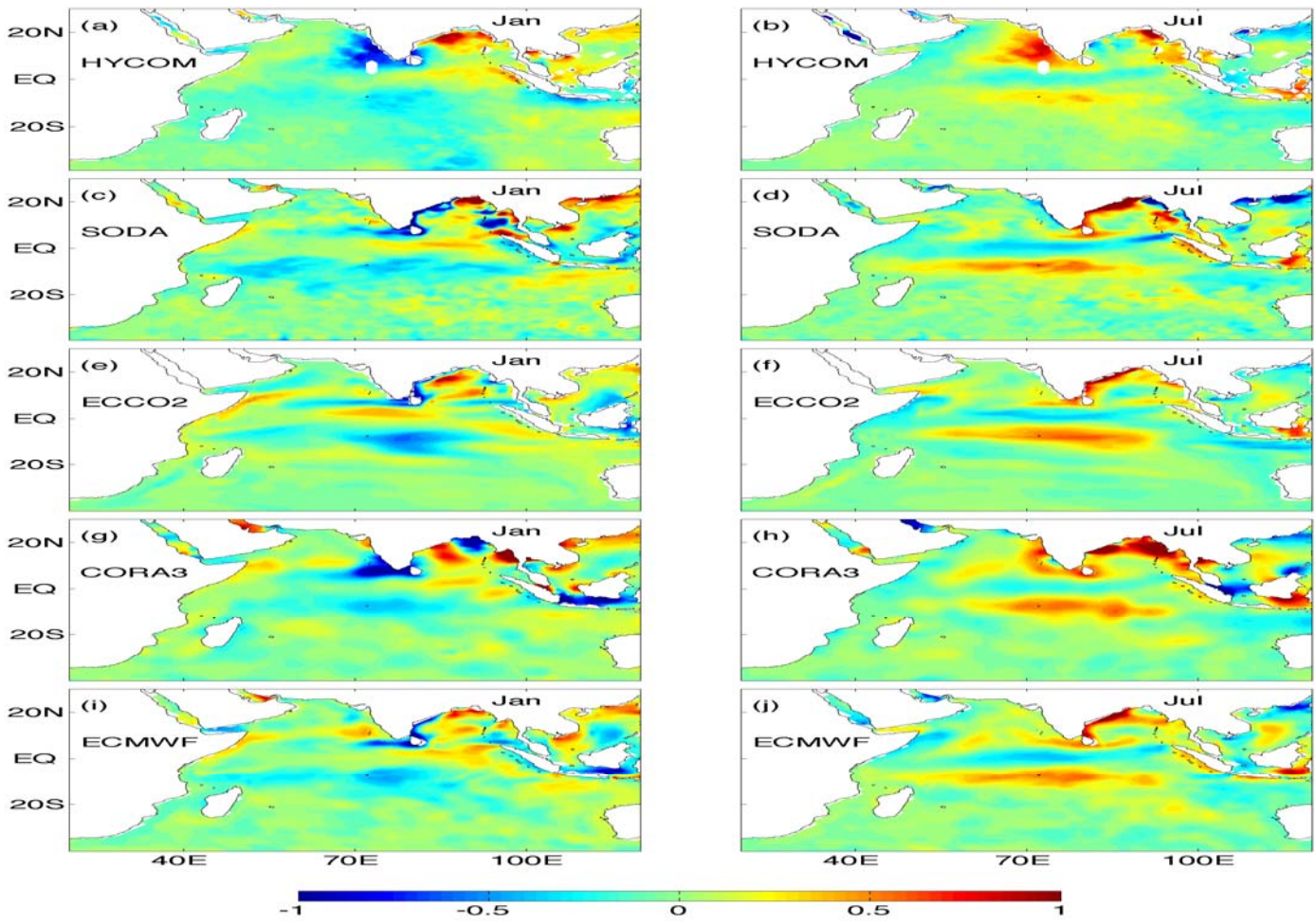

Figure 3. Mean January (left panel) and July (right panel) SSS anomalies for HYCOM (a-b), SODA (c-d), ECCO2 (e-f), CORA v3.4 (g-h), and ECMWF (i-j) averaged between January 2008 and December 2011, except SODA, which only extends out to December 2010. Anomalies were derived by subtracting the annual mean from the mean January and July spatial fields for each data set.

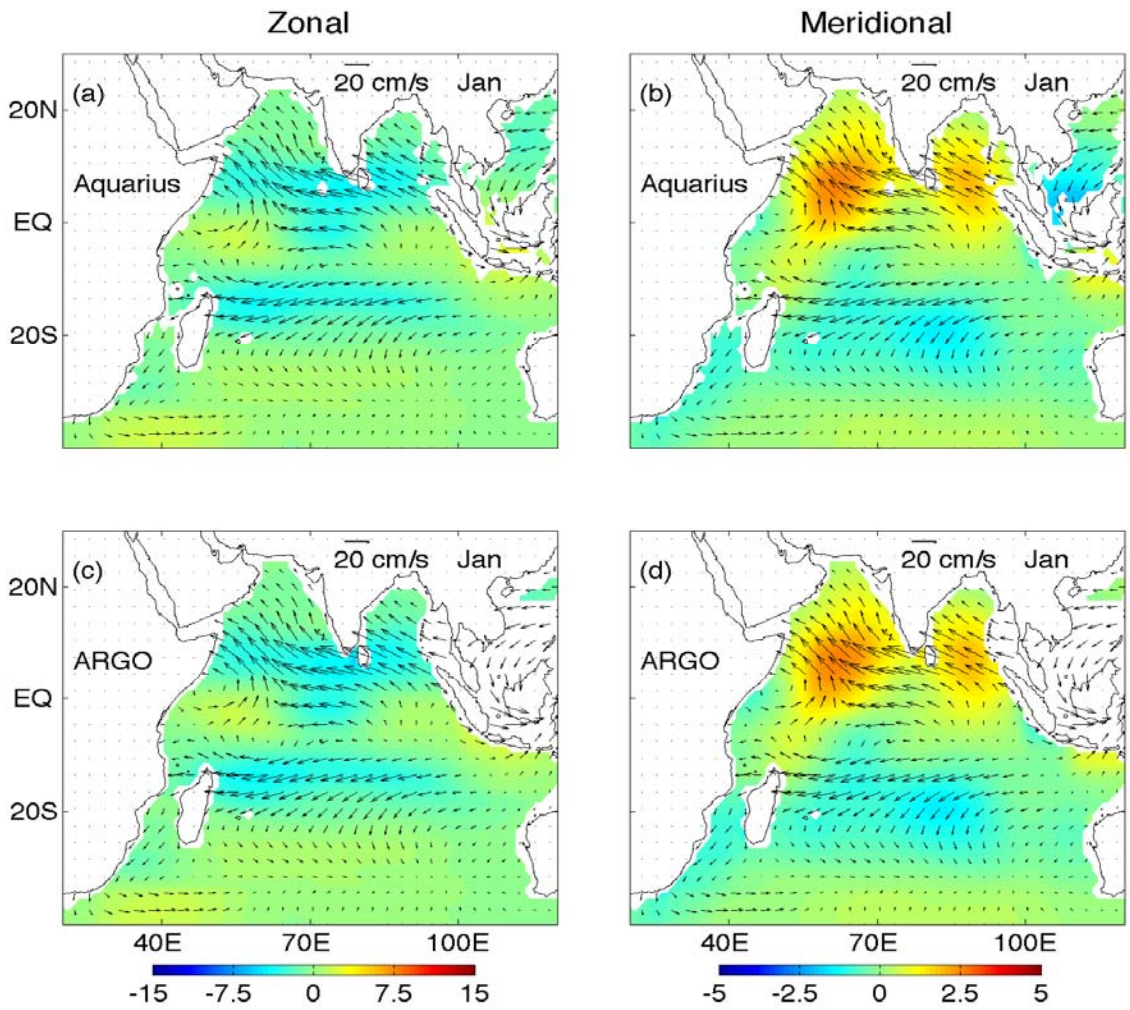

Figure 4. Mean zonal (left panel) and meridional (right panel) surface salt transports for Aquarius (top row) and Argo (bottom row) for the three Januarys between August 2011 and May 2014. Mean OSCAR currents over the same time period have been overlain to show the flow patterns. All values are in kg m^{-2} s^{-1}. Note the different color scales for zonal and meridional surface salt transports.

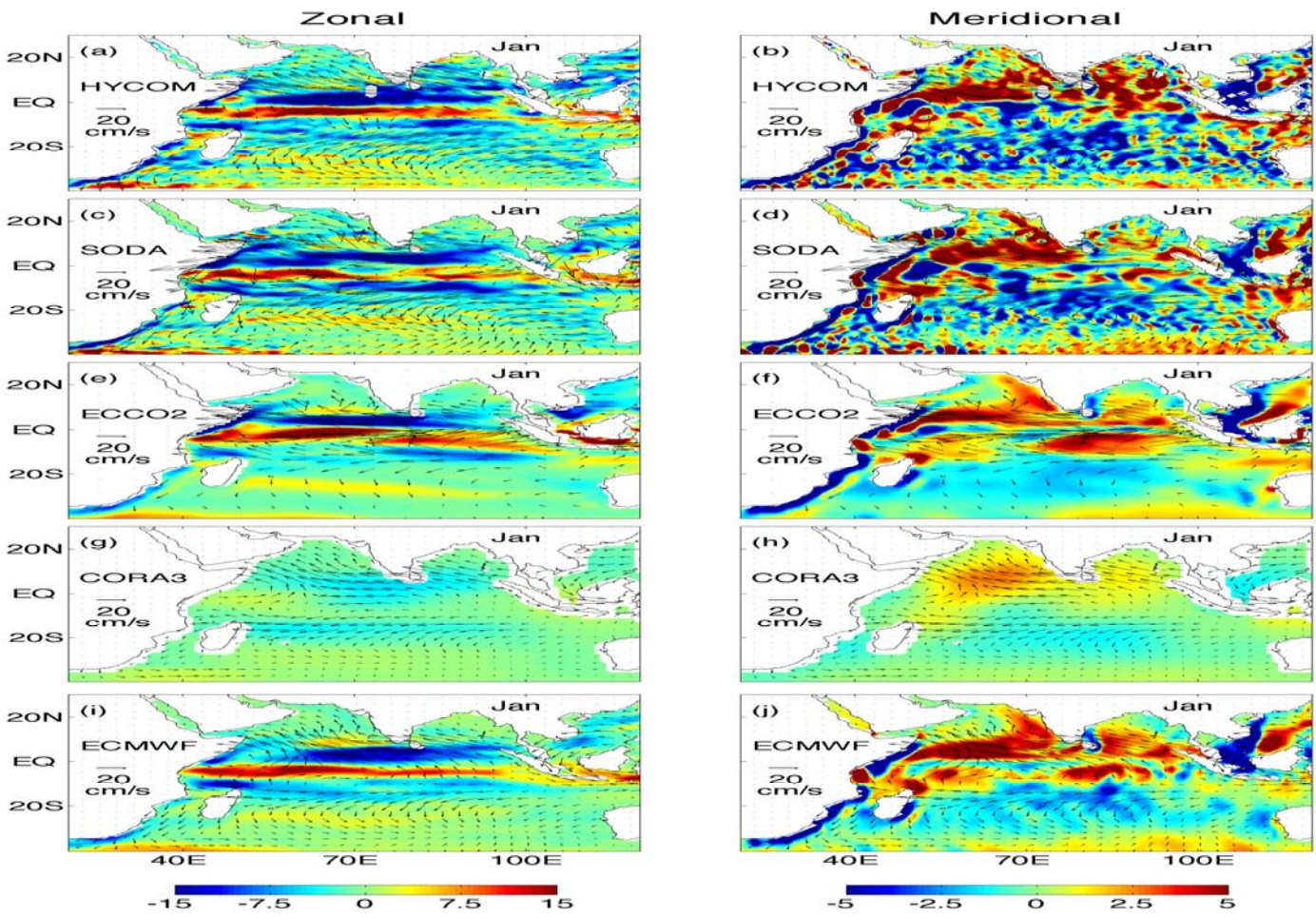

Figure 5. Mean January zonal (left panel) and meridional (right panel) surface salt transports between 2008 and 2011 for HYCOM (a-b), SODA (c-d), ECCO2 (e-f), CORA v3.4 (g-h), and ECMWF (i-j) and between 2008 and 2010 for SODA. Mean January model derived surface currents for the same time period have been overlain to show the flow pattern with the exception of CORA v3.4, which uses OSCAR currents instead. All values are in kg m^{-2} s^{-1}. Note the different color scales for zonal and meridional surface salt transports.

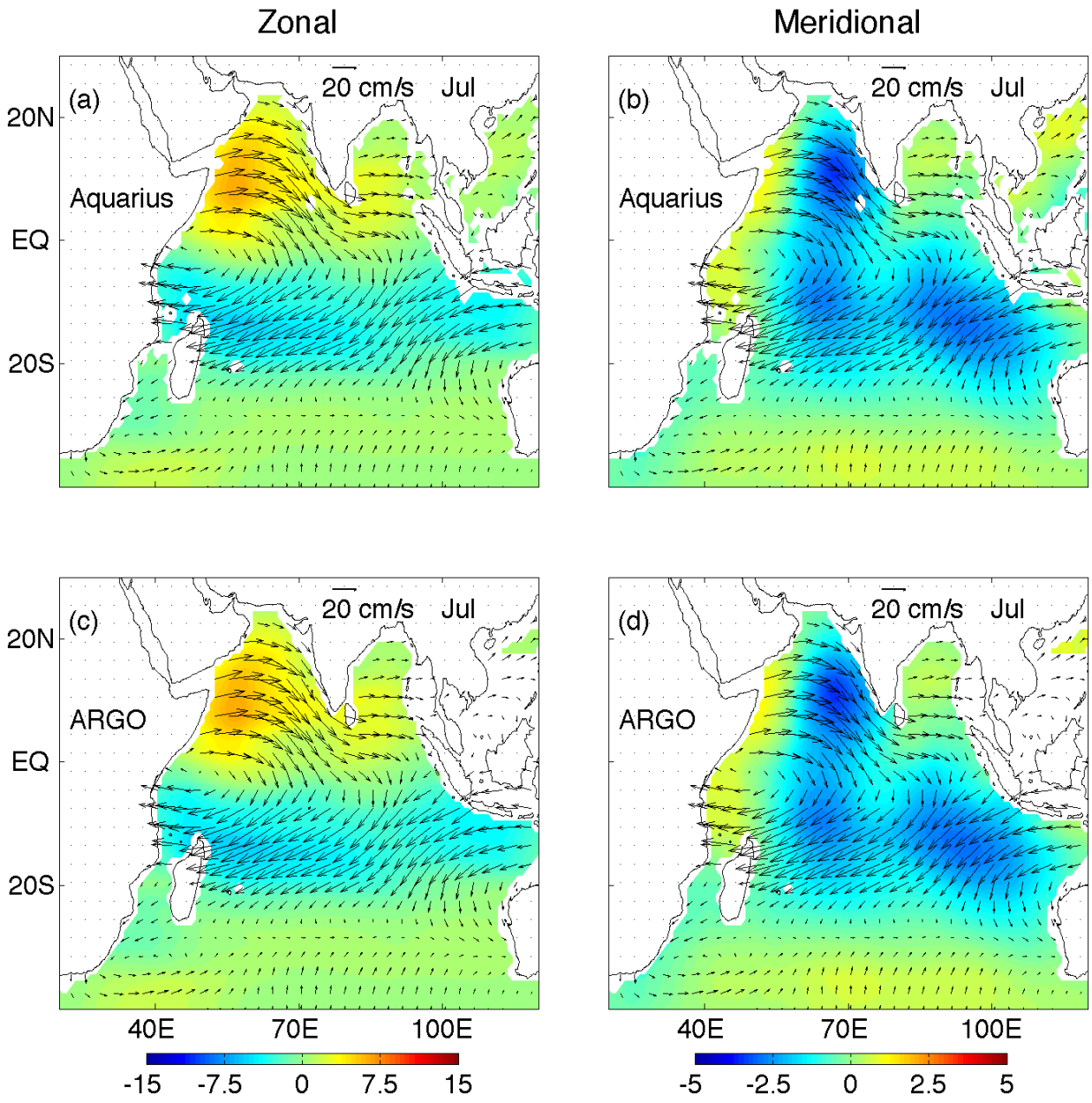

Figure 6. Mean zonal (left panel) and meridional (right panel) surface salt transports for Aquarius (top row) and Argo (bottom row) for the two Julys between August 2011 and May 2014. Mean OSCAR currents over the same time period have been overlain to show the flow patterns. All values are in kg m^{-2} s^{-1}. Note the different color scales for zonal and surface meridional salt transports.

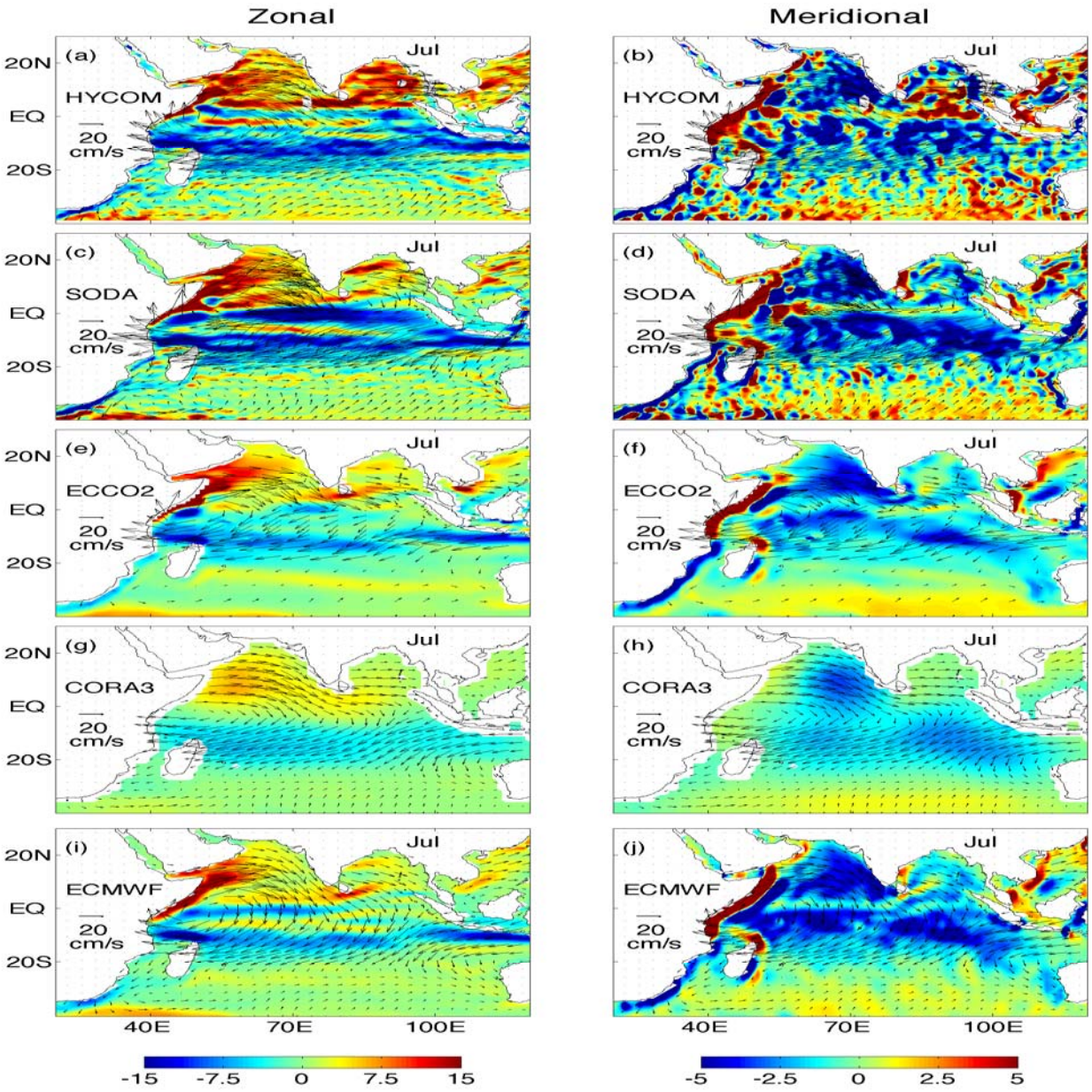

Figure 7. Mean July zonal (left panel) and meridional (right panel) surface salt transports between 2008 and 2011 for HYCOM (a-b), SODA (c-d), ECCO2 (e-f), CORA v3.4 (g-h), and ECMWF (i-j) and between 2008 and 2010 for SODA. Mean July model derived surface currents for the same time period have been overlain to show the flow pattern with the exception of CORA v3.4, which uses OSCAR currents instead. All values are in kg m^{-2} s^{-1}. Note the different color scales for zonal and surface meridional salt transports.

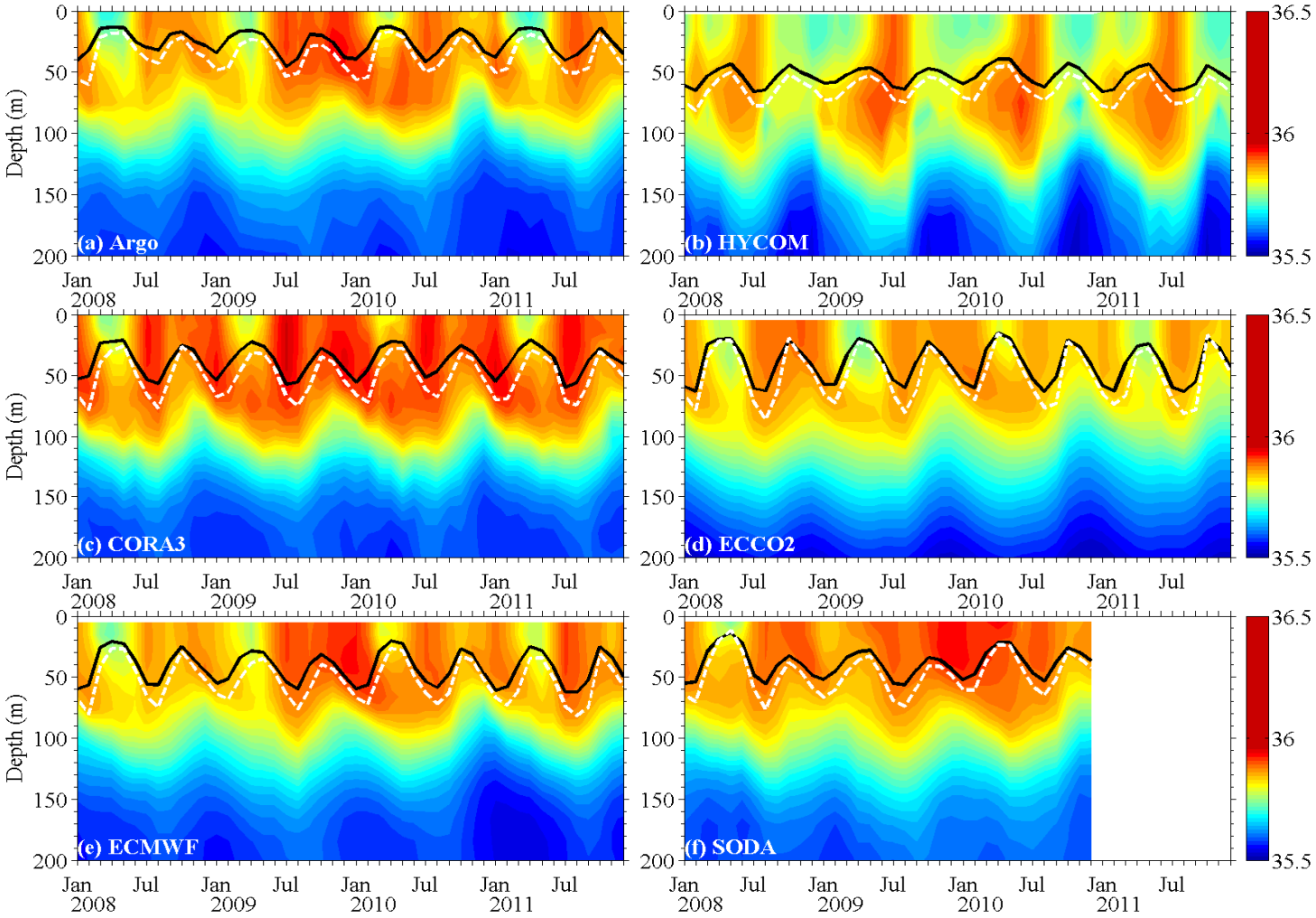

Figure 8. Time-depth sections of box-averaged salinity, mixed layer depth (m, black line), and isothermal layer depth (m, white dashed line) in the Arabian Sea between January 2008 and December 2011 from Argo (a), HYCOM (b), CORA v3.4 (c), ECCO2 (d), ECMWF (e), and SODA (f).

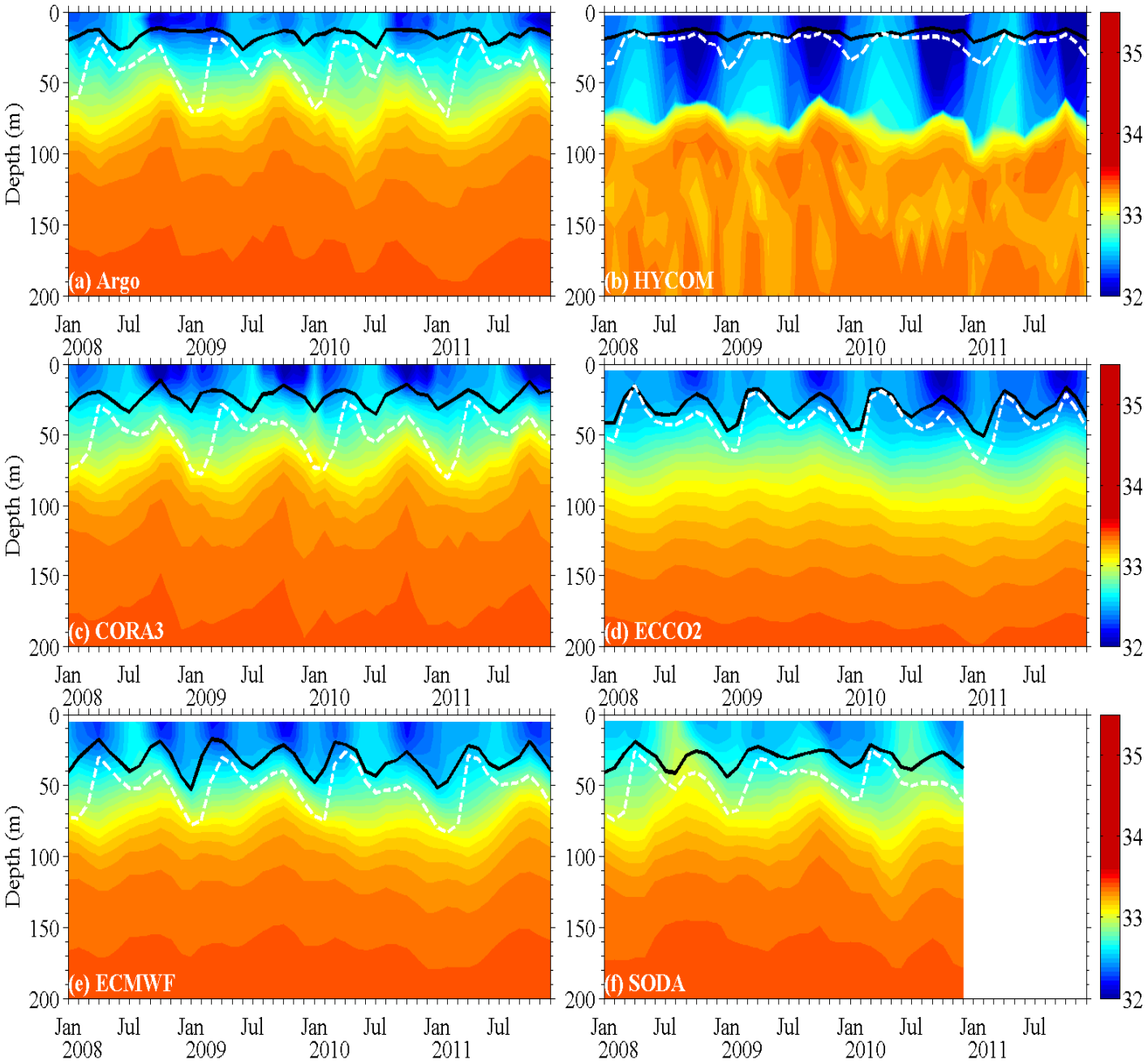

Figure 9. Time-depth sections of box-averaged salinity, mixed layer depth (m, black line), and isothermal layer depth (m, white dashed line) in the Bay of Bengal between January 2008 and December 2011 from Argo (a), HYCOM (b), CORA v3.4 (c), ECCO2 (d), ECMWF (e), and SODA (f).

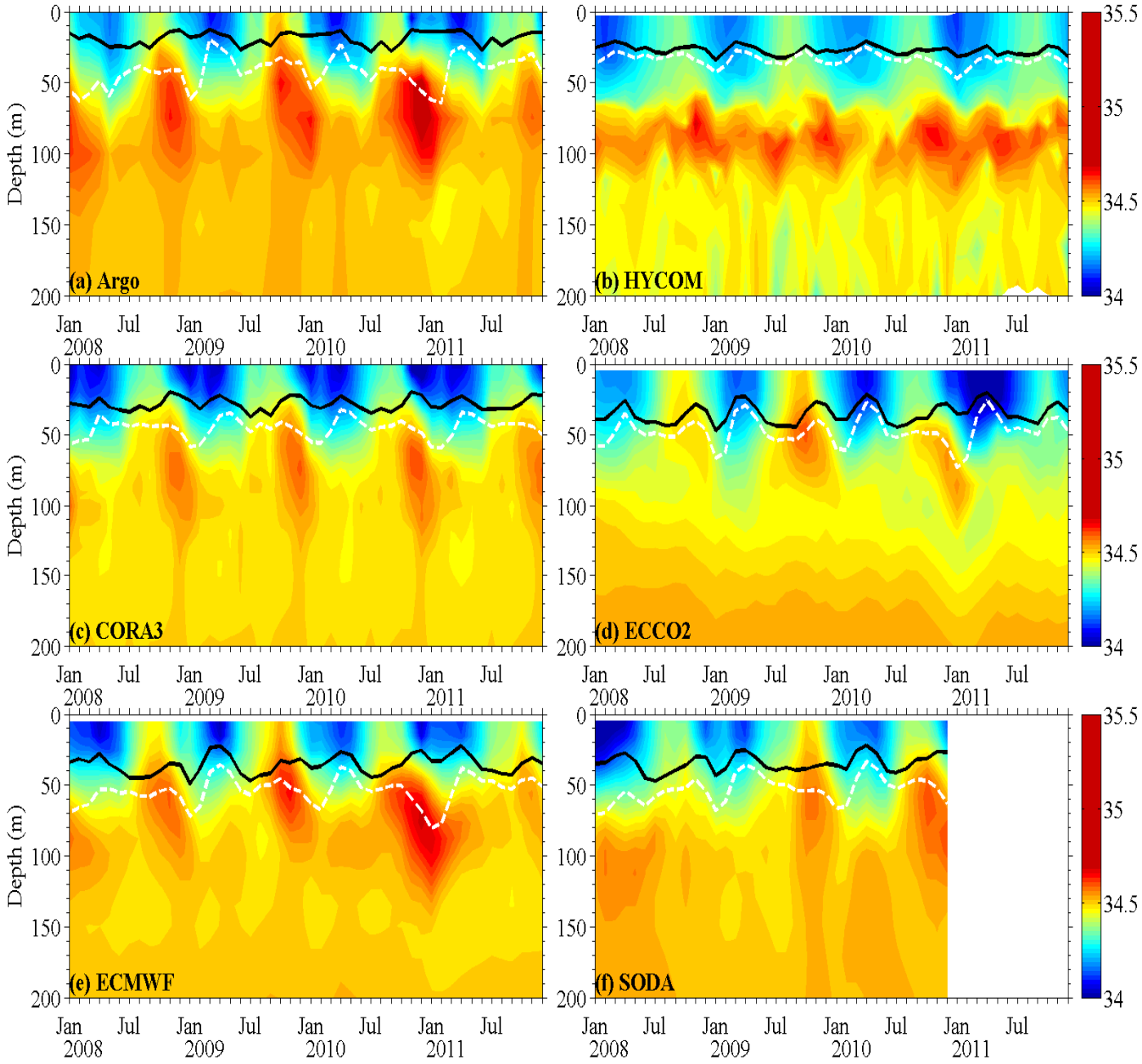

Figure 10. Time-depth sections of box-averaged salinity, mixed layer depth (m, black line), and isothermal layer depth (m, white dashed line) in the Sri Lanka box between January 2008 and December 2011 from Argo (a), HYCOM (b), CORA v3.4 (c), ECCO2 (d), ECMWF (e), and SODA (f)

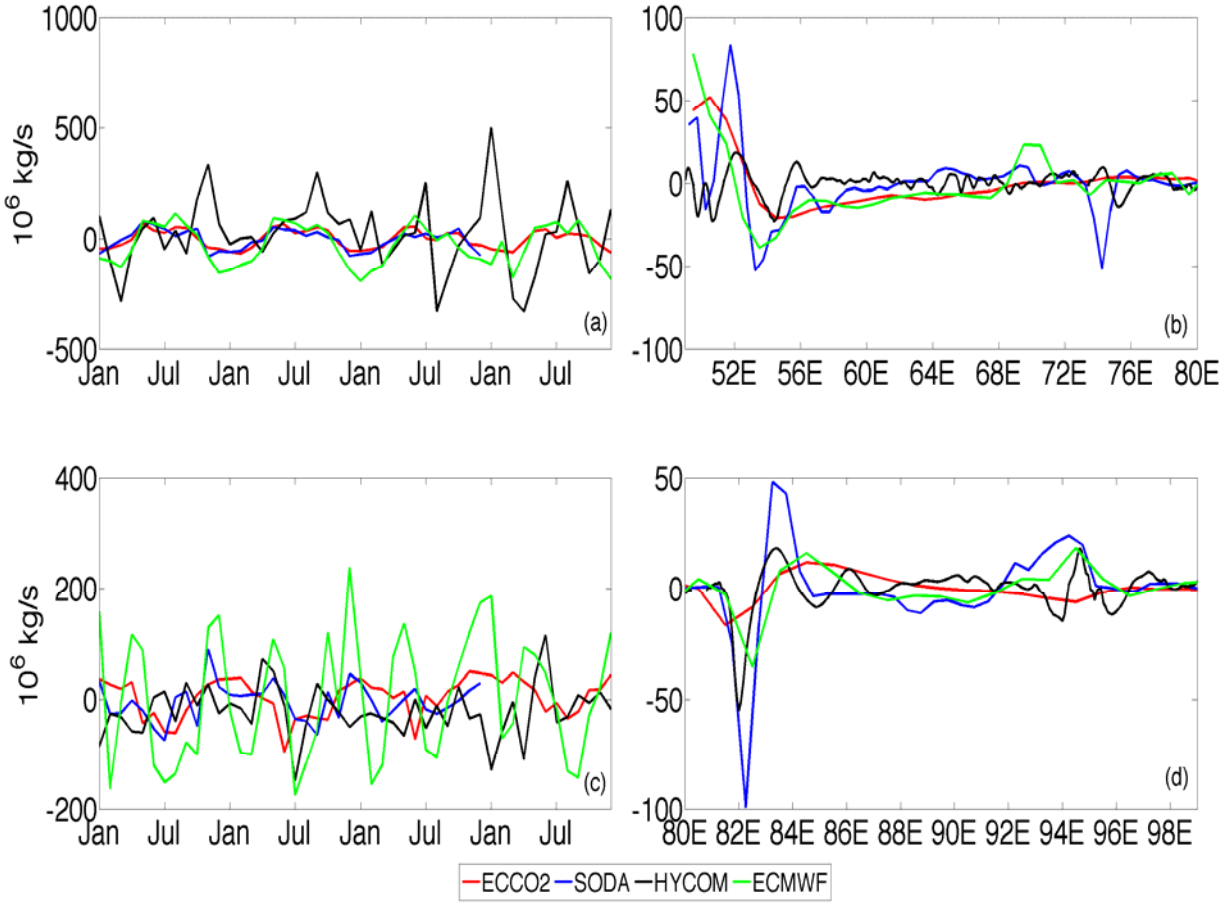

Figure 11. Monthly time-series of depth-integrated salt transports across a 6°N section in the Arabian Sea (a) and Bay of Bengal (c) between 2008 and 2011 along with depth-integrated salt transports across all lines of longitude in the Arabian Sea (b) and the Bay of Bengal (d) averaged over all months between 2008 and 2011. Salt transports are in units of $\times 10^6$ kg s^{-1}.

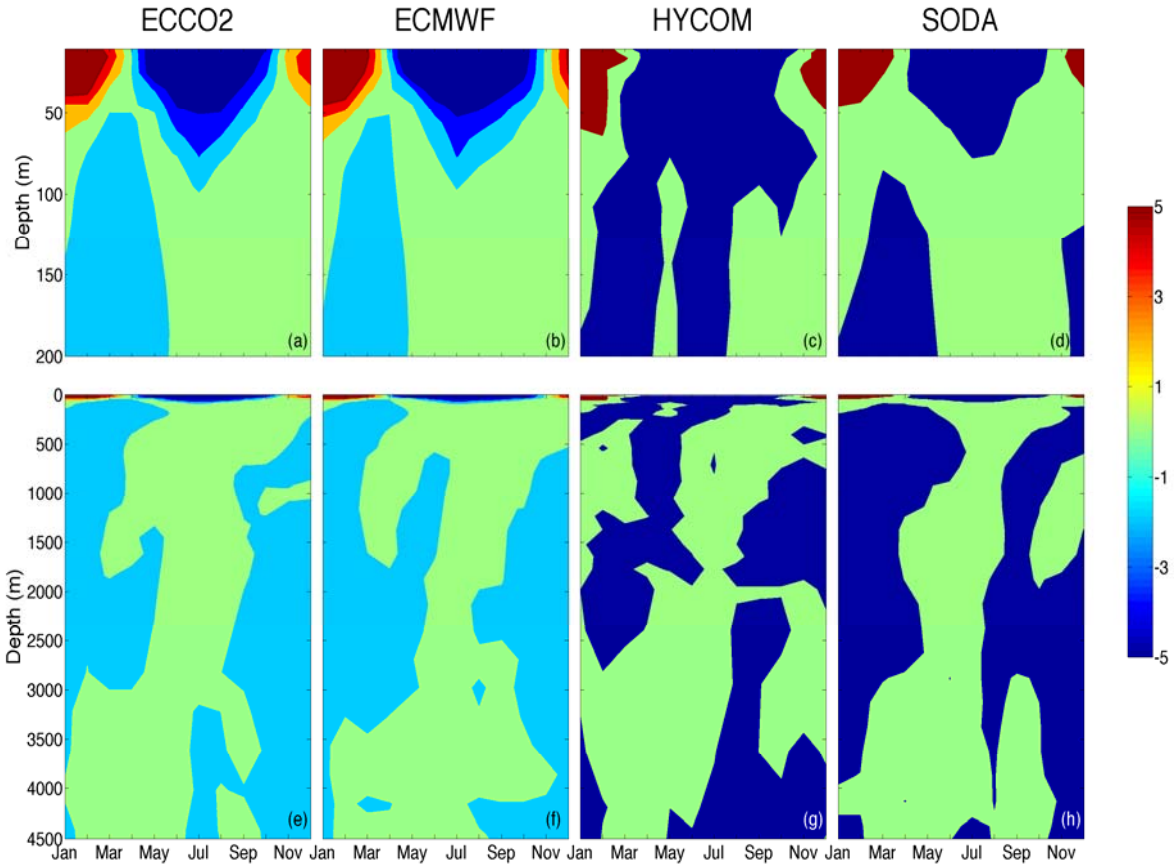

Figure 12. Depth-time plot of monthly mean salt transport per unit depth ($\times 10^6$ kg s^{-1} m^{-1}) across 6°N in the Arabian Sea over the top 200 m (a-d) and over the entire water column (e-h).

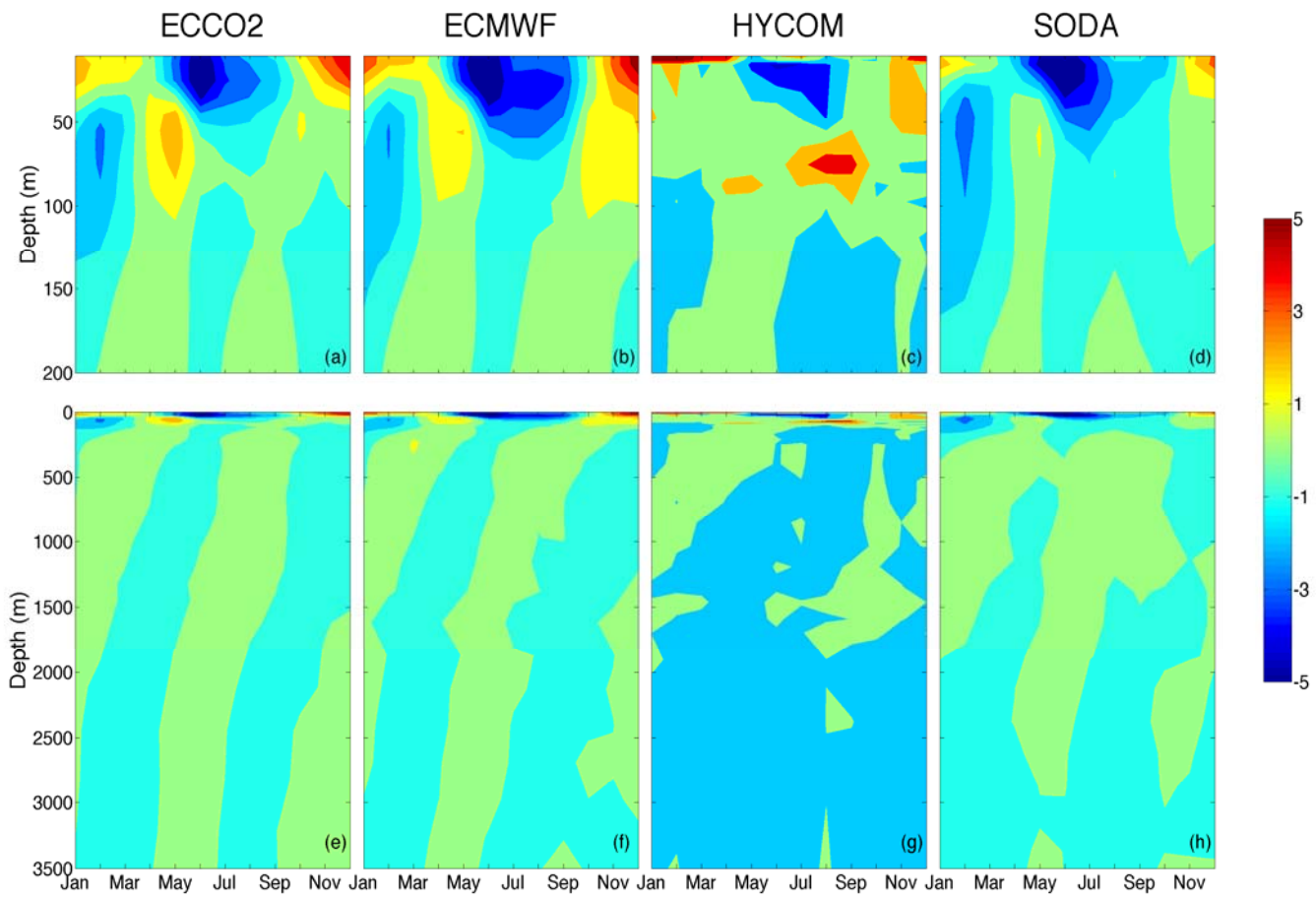

Figure 13. Depth-time plot of monthly mean salt transport per unit depth ($\times 10^6$ kg s^{-1} m^{-1}) across 6°N in the Bay of Bengal over the top 200 m (a-d) and over the entire water column (e-h).